J. Fluid Mech. (1997), *vol.* 336, *pp.* 267–299

Copyright © 1997 Cambridge University Press

Flow in two-sided lid-driven cavities: non-uniqueness, instabilities, and cellular structures

By H. C. KUHLMANN, M. WANSCHURA AND H. J. RATH
ZARM - Universität Bremen, 28359 Bremen, Germany

(Received 2 April 1996 and in revised form 6 November 1996)

The steady flow in rectangular cavities is investigated both numerically and experimentally. The flow is driven by moving two facing walls tangentially in opposite directions. It is found that the basic two-dimensional flow is not always unique. For low Reynolds numbers it consists of two separate co-rotating vortices adjacent to the moving walls. If the difference in the sidewall Reynolds numbers is large this flow becomes unstable to a stationary three-dimensional mode with a long wavelength. When the aspect ratio is larger than two and both Reynolds numbers are large, but comparable in magnitude, a second two-dimensional flow exists. It takes the form of a single vortex occupying the whole cavity. This flow is the preferred state in the present experiment. It becomes unstable to a three-dimensional mode that subdivides the basic streched vortex flow into rectangular convective cells. The instability is supercritical when both sidewall Reynolds numbers are the same. When they differ the instability is subcritical. From an energy analysis and from the salient features of the three-dimensional flow it is concluded that the mechanism of destabilization is identical to the destabilization mechanism operative in the elliptical instability of highly strained vortices.

1. Introduction

The dynamics of vortices in bounded and unbounded domains is a fundamental problem in fluid mechanics. For instance, the evolution of shear layers, reviewed by Bayly, Orszag & Herbert (1988), into two-dimensional arrays of concentrated vorticity and their subsequent three-dimensional instability has received considerable attention over many decades due to the practical importance of the subject. It is believed that the elliptic instability (Pierrehumbert 1986; Bayly 1986) is responsible for the early stages of the three-dimensional evolution of shear flows, in which the two-dimensional base flow is transient. The three-dimensional flow structures evolving from the elliptic instability may, however, be advantageously studied in a stationary closed flow system.

In this paper we consider the interaction of vortices in a closed cavity with rectangular cross-section. The vortex flow is driven by a steady motion of two facing walls tangentially in opposite directions, while the other walls are at rest. This set-up is a generalization of the well known lid-driven cavity problem (see e.g. Koseff & Street 1984) and it is similar to the so-called shear-driven cavity flow problem (see e.g. Neary & Stephanoff 1987). The extension compared to previous studies consists of introducing a second Reynolds number associated with the movement of the second

https://doi.org/10.1017/S0022112096004727 Published online by Cambridge University Press

wall, the consideration of a non-unit aspect ratio, and a long extent of the cavity in the third dimension. The same geometry has been used before, although for small and time-dependent Reynolds numbers, by Leong & Ottino (1989) and by Jana, Metcalfe & Ottino (1994) to study chaotic two-dimensional mixing.

The first major work on lid-driven cavity flow is due to Burggraf (1966). In his two-dimensional analytical and numerical study of a square cavity he found the basic vortex to develop from a viscous eddy to an inviscid rotational core at high Reynolds numbers as predicted by Batchelor (1956). In addition to the primary vortex, secondary viscous eddies (Moffatt 1964) were found to exist in the rigid corners. Pan & Acrivos (1967) investigated the dependence of the vortex structure on the aspect ratio experimentally and numerically. For small Reynolds numbers a sequence of vortices decaying exponentially with the distance from the moving lid was found as well as self-similar viscous eddies in the rigid corners. The experiments showed that the main vortex adjacent to the moving wall grows in diameter as the Reynolds number is increased and suggested a growth of the main vortex diameter like $Re^{1/2}$ for large Reynolds numbers and an infinitely deep cavity.

A series of experiments and numerical calculations for the lid-driven square cavity at higher Reynolds numbers was carried out by Freitas *et al.* (1985), Koseff & Street (1984), Koseff *et al.* (1983), Prasad & Koseff (1989), and Rhee, Koseff & Street (1984). The authors found that longitudinal Taylor–Görtler-like vortices due to a centrifugal instability appear as the first three-dimensional flow structure when the Reynolds number is increased. The size of the Taylor–Görtler-like vortices scales with the boundary layer thickness which is usually small compared to the linear dimensions of the container. On an increase of the Reynolds number these vortices become time-dependent and start to meander (Kosseff & Street 1984). These results were qualitatively confirmed by numerical benchmark calculations for unit aspect ratio and Reynolds number $Re = 3200$ presented at a GAMM-workshop (Deville, Lê & Morchoisne 1992).

Flow patterns qualitatively different from Taylor–Görtler-like vortices were found by Aidun, Triantafillopoulos & Benson (1991) in a trapezoidal shaped lid-driven cavity with a certain amount of through-flow. Spiral waves were observed that originate in the symmetry mid-plane of the cavity. These waves propagate along the secondary downstream eddy. Moreover, stationary patterns comprising a different number of cells could be established by a sudden decrease of the Reynolds number from values of $O(2000)$ to less than 500. The cells apparently scale with the cavity dimensions and fill the whole cavity.

Recently, Ramanan & Homsy (1994) investigated the stability of the basic two-dimensional lid-driven flow in a square cavity with respect to small three-dimensional perturbations. Using normal modes in the spanwise direction they found the basic flow to become unstable first at $Re = 594$ with respect to a stationary mode having a spanwise wavenumber of $k \approx 2.12$. This mode receives its energy from a well-localized region near the curved separating streamline between the primary and the secondary downstream eddy, from which it was concluded that the instability is of Görtler type. At $Re = 730$ and $k \approx 6$ another oscillatory mode was found to become destabilized to infinitesimal perturbations.

Apart from these investigations focusing on the physics of the flow in lid-driven cavities, cavity flow has become a standard benchmark problem for testing numerical codes. Goodrich, Gustafson & Halasi (1990) found two-dimensional time-periodic flow for Reynolds number $Re = 5000$ in a lid-driven cavity of aspect ratio two. Since the numerical code was restricted to two dimensions, it is unknown whether this two-

https://doi.org/10.1017/S0022112096004727 Published online by Cambridge University Press

dimensional oscillatory flow is stable with respect to three-dimensional disturbances. For an aspect ratio of one, the flow is definitely three-dimensional at $Re = 5000$.

The flow over a grooved channel, i.e. the shear-driven cavity flow problem, bears many similarities with the lid-driven cavity probem. One of the first studies on pattern formation in shear-driven cavity flow is due to Maull & East (1963). They performed experiments in a high-speed wind tunnel and found regular structures in the secondary flow inside a flush-mounted cavity in a range of parameters. Cellular patterns, time-dependent flows, and hysteresis effects were observed. These flow structures were highly dependent on the aspect ratios of the cavities used. To date, the mechanisms leading to the observed patterns are not understood.

Except for this early experimental work, most of the previous studies on shear-driven cavity flow were based on the assumption that the flow in rectangular cavities is essentially two-dimensional. Ghaddar *et al.* (1986) calculated the flow over a periodic array of grooved channels with rectangular cross-section using a spectral-element method. For small Reynolds numbers the flow consists of an outer channel flow and a recirculating flow in the cavities being separated from the outer flow by a free shear layer. Their two-dimensional linear stability calculation showed, that Tollmien–Schlichting-like waves triggered by a Kelvin–Helmholtz instability appear above a critical Reynolds number. Amon & Patera (1989) performed numerical simulations of the three-dimensional grooved channel flow. They found that the primary Tollmien–Schlichting wave instability is supercritical in contrast to plane Poiseuille flow. The two-dimensional wave becomes unstable to a three-dimensional excitation that is interpreted as a slightly detuned classical channel secondary instability.

On the experimental side, Neary & Stephanoff (1987) investigated the shear-driven flow over a single shallow cavity. They found shear layer oscillations similar to those studied by Ghaddar *et al.* (1986). In addition to the basic frequency associated with this instability another frequency appeared slightly above the first threshold Reynolds number. This latter frequency was attributed to a wave running spanwise on the separated vortex in the cavity.

Here, we investigate the two-dimensional flow and its linear instability with respect to three-dimensional perturbations in a two-sided lid-driven cavity. In §2 the experimental set-up is described. Section 3 deals with the numerical techniques. The experimental and numerical results will be presented in §4. In §5 the results are discussed and compared with phenomena in unbounded flows.

2. Experimental set-up

Experimental studies of lid-driven cavity flow are usually carried out using the simplest geometry, namely a container with rectangular cross-section. This simple geometry is also well suited to a comparison with numerical calculations. The technical realization of appropriate boundary conditions is facilitated, however, if a slight wall curvature is allowed. Therefore, we use rigid rotating cylinders of large radii as moving lids in our experiment, similar to Aidun *et al.* (1991) and Pan & Acrivos (1967). It is expected that the flow and its stability properties are only marginally influenced in most cases by the imperfection of the moving walls being cylindrical rather than plane.

The set-up is shown schematically in figure 1. The cavity is bounded vertically by two parallel Plexiglas plates of thickness 9.4 mm and width in the x-direction of (58 ± 0.05) mm. The vertical spacing h=(29.0 ± 0.1) mm in the y-direction between the top and the bottom stationary lids will be used as the reference length scale. The lateral

https://doi.org/10.1017/S0022112096004727 Published online by Cambridge University Press

boundaries of the cavity are formed by two chrome-plated metal cylinders of radii R_1=(87.55 $\pm$ 0.03) mm and R_2=(88.25 $\pm$ 0.03) mm, respectively. Both cylinders can be rotated independently around fixed horizontal parallel axes. They are in contact with the stationary top and bottom lids along their respective edges. The minimum horizontal distance between both cylinders is (55.4 $\pm$ 0.1) mm while the average horizontal width of the cavity is d=(56.7 $\pm$ 0.1) mm. This average value will be used in the numerical calculations as the width of an equivalent strictly rectangular cavity. The vertical spacing is enforced by thick front and rear Plexiglas windows of height h. The length of the cavity in the z-direction is l=(190.0 $\pm$ 0.1) mm. Thus, the geometry of the cavity is specified by the two aspect ratios

$$\Gamma = \frac{d}{h} = 1.96 \pm 0.05 \qquad \text{and} \qquad \Lambda = \frac{l}{h} = 6.55\ . \tag{2.1}$$

The lateral sides of both windows are machined to match the radii of the moving cylinders. All parts forming the cavity are mounted in an open rectangular container. The front and rear windows as well as the bearings of the cylinders' axes are fixed on the sidewalls of the outer container. The bearings can be shifted slightly perpendicular to the axes to enable the adjustment of the cavity. In this way the small gaps between stationary and moving parts can be minimized in order to reduce through-flow effects. The remaining gaps were nowhere larger than 40 μm. To avoid the accumulation of air bubbles in the interior of the cavity due to a residual pumping effect, the outer container, into which the cavity is immersed, is filled with the same liquid. Observation of the flow is possible through the front window as well as through the upper stationary lid. To prevent liquid from the bath spilling on the upper lid, it is framed with a vertical shaft, which also gives it additional stability. The cylinders are independently driven via tooth belts by two computer-controlled permanent-magnet synchrone motors. The working fluid used was Bayer 'Baysilone M20' silicone oil of kinematic viscosity $\nu = 0.236$ cm^2 s^{-1} at $T = 20$°C. Since the kinematic viscosity may change due to a temperature variation of a few degrees during a day of operation, the temperature of the liquid bath was permanently measured by a thermocouple and the Reynolds numbers

$$Re_i = \frac{\Omega_i R_i h}{\nu} \tag{2.2}$$

were periodically updated to keep them at their prescribed values. The relative error in Re_i is estimated to be less than 1%. Flow visualization was accomplished by adding small amounts of aluminium particles to the liquid. A thick light sheet mounted horizontally and entering the cavity through the front window was used to view the flow from above. A vertical light sheet through the top lid allowed the cross-section of the flow to be viewed from the front window. Since the transition between different flow patterns is in most cases characterized by a sudden jump, visual observation was sufficient to detect the transition points within the accuracy of the given pair of Reynolds numbers. If not mentioned otherwise the error is within the size of the plotted symbols. Several tests have been made regarding the influence of the gap width between the stationary and moving boundaries. By lifting the upper lid in a defined manner the height of the cavity was artificially increased by up to 0.6 mm. A change in the relative size of the resulting gaps did not change qualitatively the experimental results.

https://doi.org/10.1017/S0022112096004727 Published online by Cambridge University Press

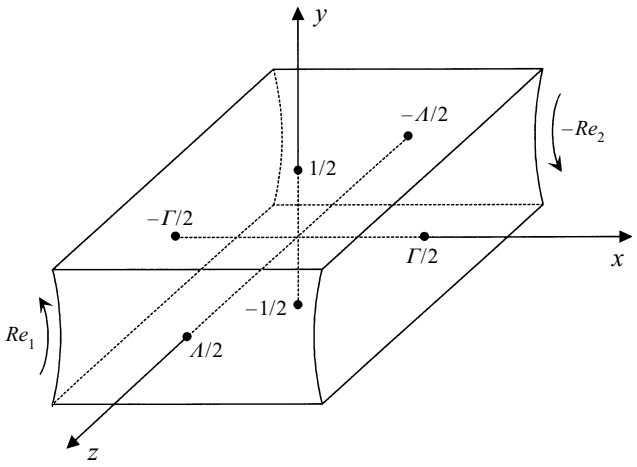


FIGURE 1. Sketch of the cavity and coordinate system.

3. Numerical methods

For a numerical analysis of the nonlinear cavity flow we use the model of an incompressible Newtonian fluid. The Navier–Stokes and continuity equation for the velocity $\boldsymbol{u} = (u, v, w)$ and pressure p are

$$\partial_t \boldsymbol{u} + \boldsymbol{u} \cdot \nabla \boldsymbol{u} = -\nabla p + \nabla^2 \boldsymbol{u} \,, \tag{3.1a}$$

$$\nabla \cdot \boldsymbol{u} = 0 \,, \tag{3.1b}$$

where we have used the viscous scales $h, h^2/\nu, \nu/h$, and $\rho\nu^2/h^2$ for length, time, velocity and pressure, respectively. The conditions imposed on the boundary of the rectangular domain occupied by the fluid (figure 1) are

$$v = \begin{cases} Re_1 \\ -Re_2 \end{cases} \quad \text{on} \quad x = \begin{cases} -\Gamma/2 \\ +\Gamma/2 \end{cases} \,, \tag{3.2a,b}$$

$$u = w = 0 \quad \text{on} \quad x = \pm\Gamma/2 \,, \tag{3.2c,d}$$

$$\boldsymbol{u} = 0 \quad \text{on} \quad y = \pm 1/2 \,, \tag{3.2e,f}$$

and the periodicity condition in the z-direction involving the wavelength λ as a parameter

$$\boldsymbol{u}(z) = \boldsymbol{u}(z + \lambda) \,. \tag{3.3}$$

The end condition in the experiment corresponds to

$$\boldsymbol{u} = 0 \quad \text{on} \quad z = \pm\Lambda/2 \,. \tag{3.4}$$

The Navier–Stokes equations (3.1*a*, *b*) have been unconventionally non-dimensionalized by constant diffusive scales, because a scaling using either one of the two different Reynolds numbers cannot appropriately describe the velocity scale for arbitrary Reynolds number combinations with $Re_1 \neq Re_2$. Moreover, the introduction of the additional parameter Re_1/Re_2 is avoided.

The numerical methods used to calculate the steady two-dimensional basic flow ($\partial_t = \partial_z = w = 0$) and its linear stability with respect to arbitrary time-dependent disturbances are identical to those employed by Wanschura *et al.* (1995) to calculate the stability of toroidal vortex flows in cylindrical volumes, except for minor modifications to adapt the code to a Cartesian rather than a cylindrical coordinate

https://doi.org/10.1017/S0022112096004727 Published online by Cambridge University Press

system. The reader is referred to Wanschura *et al.* (1995) for details of the numerical treatment. In the following the solution methods are briefly summarized.

These basic flows ($\boldsymbol{u}_0 = (u_0, v_0, 0), p_0$) are calculated using a second-order finite difference method on an equidistant grid in the y-direction and a Chebyshev collocation method on Gauss–Lobatto points in the x-direction. The discretized set of nonlinear equations for the unknowns is solved by Newton–Raphson iteration. Once a basic state is obtained, it is used as the parametric input for a linear stability analysis. The linearized equations for the deviations $(\boldsymbol{u}, p)$ from the basic state

$$\partial_t \boldsymbol{u} + \boldsymbol{u}_0 \cdot \nabla \boldsymbol{u} + \boldsymbol{u} \cdot \nabla \boldsymbol{u}_0 = -\nabla p + \nabla^2 \boldsymbol{u} \,, \tag{3.5a}$$

$$\nabla \cdot \boldsymbol{u} = 0 \,, \tag{3.5b}$$

subject to no-slip and no-penetration boundary conditions on the rigid walls and periodic boundary conditions in the z-direction (3.3) are solved using normal modes

$$\begin{pmatrix} u(x,y,z,t) \\ v(x,y,z,t) \\ w(x,y,z,t) \\ p(x,y,z,t) \end{pmatrix} = \begin{pmatrix} \hat{u}(x,y) \\ \hat{v}(x,y) \\ \hat{w}(x,y) \\ \hat{p}(x,y) \end{pmatrix} \mathrm{e}^{(\sigma t + \mathrm{i}kz)} + \text{c.c.} \,, \tag{3.6}$$

where $k = 2\pi/\lambda$ is the disturbance wavelength. The same discretization as for the basic state is applied to (3.5) to obtain linear algebraic equations for $(\hat{u}, \hat{v}, \hat{w}, \hat{p})$. The resulting generalized eigenvalue problem is solved by IMSL routines calculating all eigenvalues σ (complex growth rates). Once the most dangerous mode has been identified, the respective eigenvalue is traced by inverse iteration. The neutral mode and the stability boundary are found by varying Re_1 and Re_2 such that $\mathrm{Re}(\sigma) = 0$.

The discontinuity of the boundary conditions in the corners between stationary and moving boundaries requires special attention. Koplik & Banavar (1995) showed that a realistic continuum modelling of the corner region should take into account a local non-Newtonian behaviour to remove the stress singularities at ($x = \pm\Gamma/2,\ y = \pm 1/2$). To overcome this difficulty the problem is regularized by using the boundary conditions

$$v = \begin{cases} \frac{1}{4}\left[1 - \cos\left(10\pi\left(y + \frac{1}{2}\right)\right)\right]^2 & \text{if} \quad y \leqslant -0.4 \\ 1 & \text{if} \quad -0.4 \leqslant y \leqslant 0.4 \\ \frac{1}{4}\left[1 - \cos\left(10\pi\left(y - \frac{1}{2}\right)\right)\right]^2 & \text{if} \quad y \geqslant 0.4 \end{cases} \times \begin{cases} Re_1 \\ -Re_2 \end{cases} \quad \text{on} \quad x = \begin{cases} -\Gamma/2 \\ +\Gamma/2 \end{cases} , \tag{3.7a,b}$$

instead of (3.2*a*,*b*). This regularization is much less severe than that employed previously by Shen (1991). Test calculations yielded a difference in the critical Reynolds number for symmetrical driving ($Re_1 = Re_2$) of less than 0.01% when the smoothing region at each corner is reduced from 10% to 2.5%. The grid convergence of the two-dimensional base flow and the linear stability analysis is found to depend on the Reynolds numbers and on the particular base state under investigation. Using 100 vertical finite difference and 30 horizontal Chebyshev collocation points the numerical error in the critical values is estimated to be less than 0.5% for the cat's eye flow, while the error is less than about 3% for the two-vortex state, which exhibits higher velocity gradients. Both types of base flow will be defined further below. The error estimates have been obtained by comparison with calculations using 200 by 40 grid points.

https://doi.org/10.1017/S0022112096004727 Published online by Cambridge University Press

4. Results

For a comparison of experimental and numerical results it must be kept in mind that the boundary condition (3.4) corresponding to the experiment is different from the periodic boundary condition (3.3) used in the numerical calculations. While the experimental flow is always three-dimensional there exist two-dimensional flows for (3.3).

The three-dimensionality of the experimental flow is caused by the rigid boundary conditions on $z = \pm\Lambda/2$. The endwall-induced flow has distinct characteristics. In the limit of creeping flow deviations from the ideal two-dimensional flow will decay exponentially with the distance from the sidewalls on a characteristic length scale of $O(1)$ (in the present units). In addition, for high Reynolds numbers inertial effects will lead to a secondary flow of Bödewaldt type (Bödewaldt 1940). The axial velocity w can become quite strong even away from the endwalls. Therefore, the flow is two-dimensional only in the midplane $z = 0$ due to its mirror symmetry. Owing to the deceleration effect of the endwalls the flow velocities in the midplane, however, are generally smaller than in the absence of endwalls (de Vahl Davis & Mallinson 1976).

Here we are interested in the bulk fluid motion far away from the endwalls. In order that the three-dimensional endwall-induced flow at given Reynolds numbers be vanishingly small, one would have to consider the central regions near $z \approx 0$ in cavities with increasingly large aspect ratios Λ. Therefore, endwall effects cannot be avoided in practice. In many cases they are, however, sufficiently small beyond a distance of a few characteristic length scales from the endwalls. A similar problem arises, e. g., in experimental realizations of the Taylor–Couette problem, in which Ekman vortices are induced by the rigid collars axially bounding the annular gap (Alziary de Roquefort & Grillaud 1978; Di Prima & Swinney 1981).

Our comparison of the two-dimensional numerical solutions with the three-dimensional cavity flow is based on the assumption that the secondary endwall-induced three-dimensional flow is only a small perturbation of the two-dimensional primary flow in the central part of the cavity. The validity of this assumption can be assessed by comparing calculated two-dimensional velocity profiles with the corresponding measured velocity fields. An example is given in figure 5 below. From our measurements and visual observations we conclude that the experimental flow near in the centre of the cavity is quasi-two-dimensional and may be reasonably well described by the two-dimensional numerical solution.

In the following we consider steady flows and both Reynolds numbers being positive. Then the left wall moves upward while the right wall moves downward as indicated in figure 1.

4.1. *Two-dimensional flows, $Re_1 = Re_2$*

In §§4.1–4.5 we consider the case when both Reynolds numbers are equal. For brevity we denote $Re = Re_1 = Re_2$. Any changes of the Reynolds numbers in the experiment have been made quasi-steadily and simultaneously for both Re_1 and Re_2. For $\Gamma = 1.96$ and small Reynolds number the flow in the midplane of the cavity is steady and consists of two vortices co-rotating in a clockwise direction. The numerical streamlines for Stokes flow are shown in figure 2(*a*). On increasing the Reynolds number up to $Re \approx 200$ the strength of both vortices increases, but their shapes do not change qualitatively. Streamlines of the steady flow in a vertical cross-section at $z = 0$ are shown in figure 2(*b*) for $Re = 230$. The projection of the experimental streamlines onto the (x, y)-plane is nearly constant over most z-stations

https://doi.org/10.1017/S0022112096004727 Published online by Cambridge University Press

of the cavity. Minor changes are visible only close to the endwalls at $z = \pm\Lambda/2$. The corresponding numerically calculated two-dimensional streamlines for a similar Reynolds number ($Re = 240$) are displayed in figure 2(c). Both patterns show a good agreement. It is also seen that the flow pattern at $Re = 230$ does not deviate much from the Stokes flow pattern (figure 2a): the vortices become slightly asymmetric with respect to $y = 0$, their diameter in the x-direction decreases with Re, and two small regions of separated flow appear on the stationary walls, within which the fluid is nearly stagnant ($\psi_{min} = -26.29,\ \psi_{max} = 0.142$).

As the Reynolds number is further increased quasi-statically in small steps (the time interval between successive variations of Re was 2 min, roughly corresponding to the lateral momentum diffusion time $\tau_d = d^2/\nu$), a jump transition occurs in the experiment at $Re^{(0+)} = 232$ to a flow state in which the two distinct vortices get involved with each other and partly merge. There remain two small regions which, in the projection, appear as nearly closed streamlines separated by a separatrix streamline around which most of the flow is circulating clockwise (figure 3a). The interior region of separated flow is characterized by two elliptical and one hyperbolic stagnation point and takes the form of cat's eyes. The main part of the cat's eye flow is topologically equivalent to the two-vortex flow. On a quasi-steady decrease of the Reynolds numbers the flow switches back from the cat's eye to the two-vortex state at $Re^{(0-)} = 224$, thus forming a hysteresis loop. Since the fluid motion is unique in the limit of vanishing Reynolds number, the appearance of the cat's eye flow must be an inertial effect. The cat's eye flow is essentially two-dimensional, except for a small region of extent $\lesssim 1$ in the z-direction from the endwalls at $z = \pm\Lambda/2$. The projection of the streamlines onto the (x, y)-plane changes from the cat's eye pattern in the bulk to the basic two-vortex pattern in the direct vicinity of the endwalls.

The observed experimental behaviour is consistent with the structure of the solution manifold of the two-dimensional numerically calculated flow. The two-vortex solution was traced by increasing the Reynolds number in small steps (typically $\Delta Re = 20$) using the previously calculated solution as the initial guess for the Newton iteration. At $Re = 427 \pm 5$ (for a grid resolution of 100×45) the Newton iteration ceased to converge even for Reynolds number increments as small as $\Delta Re = 1$. The breakdown of the iteration can be understood by examining the behaviour of some flow quantity as a function of Γ and Re. It is found that the solution surface is locally s-folded. The fold is illustrated in figure 4, where we have plotted the shear stress on the moving wall at $x = \Gamma/2,\ y = 0$ as a function of the Reynolds number for $\Gamma = 1.96$. The solution curve turns back sharply at $Re^{(0+)} = 427$ and turns forward again at $Re^{(0-)} = 234.3$. The solutions in the region of non-uniqueness belonging to high (cat's eye flow) and low (two-vortex flow) shear stress on the moving wall have been found by varying Γ at constant Re. The solution with intermediate shear stress has been obtained by random initial perturbation of the cat's eye flow solution. A stability analysis reveals that both the two-vortex and the cat's eye flow state are linearly stable to infinitesimal two-dimensional disturbances, whereas the solution with intermediate shear stress is unstable. The streamlines of the unstable solution (not shown) look like an average of the cat's eye and two-vortex patterns.

The numerically calculated streamlines corresponding to the cat's eye state are plotted in figure 3(b) for $Re = 257$, which corresponds to neutral three-dimensional stability (see §4.2). These streamlines are very close to the numerical ones for $Re = 233$ and they also show a good agreement with the experimental result at the midplane (figure 3a). Vertical velocity profiles $v(x, y = 0)$ of the two-vortex ($Re = 200$) and the cat's eye flows ($Re = 240$) at a distance $\Delta z = 1.7$ from the endwall are plotted

https://doi.org/10.1017/S0022112096004727 Published online by Cambridge University Press

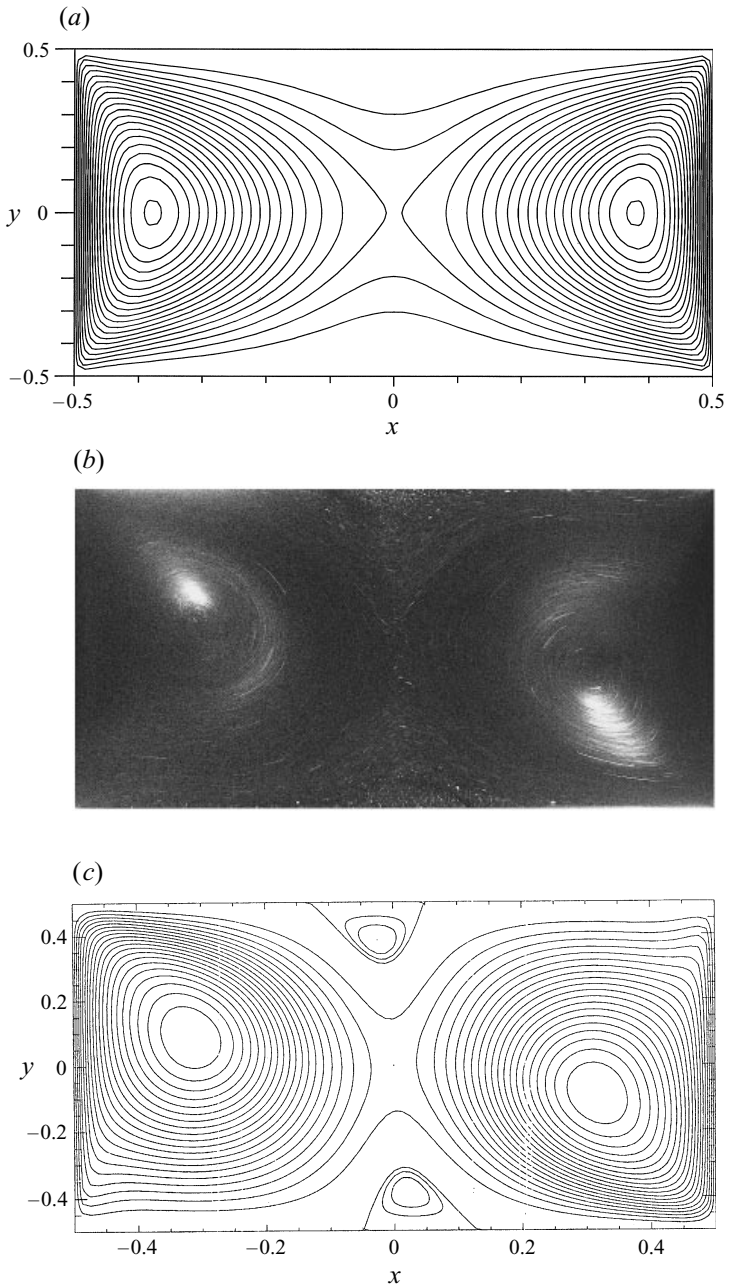


FIGURE 2. Basic flow for $\Gamma = 1.96$ and symmetrical driving $Re = Re_1 = Re_2$. (*a*) Numerical streamlines of the Stokes flow. (*b*) Projection of the experimental streamlines at $z = 0$ for $Re = 230$. (*c*) Numerical streamlines for $Re = 240$ (The streamlines have been rescaled in the separated region for better visibility.) The x-axis is scaled in units of d.

in figure 5. The numerical data for the two-vortex flow compare well with the experimental data. There is also a reasonable agreement between the numerical cat's eye solution and the measured values.

https://doi.org/10.1017/S0022112096004727 Published online by Cambridge University Press

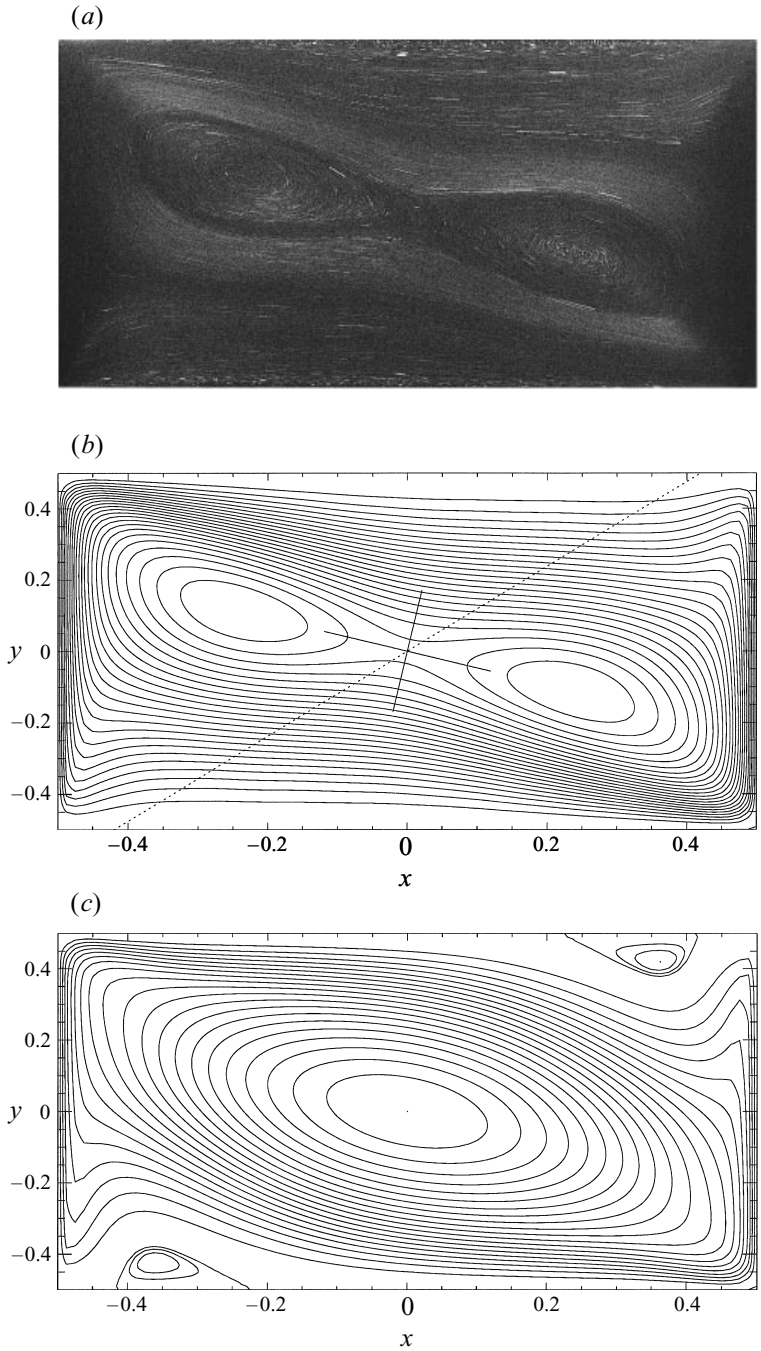


FIGURE 3. Basic cat's eye flow for $\Gamma = 1.96$ and symmetrical driving $Re = Re_1 = Re_2$. (*a*) Projection of the experimental streamlines at $z = 0$ for $Re = 233$. (*b*) Numerical cat's eye solution for $Re = 257$. The full straight lines represent local coordinate axes and the dotted line is the strain direction at $x = y = 0$. (*c*) Numerical cat's eye solution for $Re = 800$. The x-axes are scaled by d.

https://doi.org/10.1017/S0022112096004727 Published online by Cambridge University Press

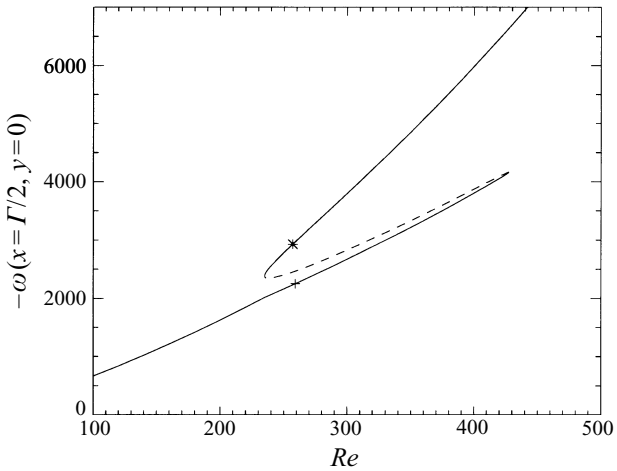


FIGURE 4. Shear stress $\omega := \partial v/\partial x$ at $(x = \Gamma/2, y = 0)$ as a function of the Reynolds number for $\Gamma = 1.96$. The dashed line indicates an unstable solution. The asterisk and the plus mark the linear stability boundaries of the cat's eye flow ($Re^{(1)}$) and the two-vortex flow ($Re^{(2)}$), respectively.

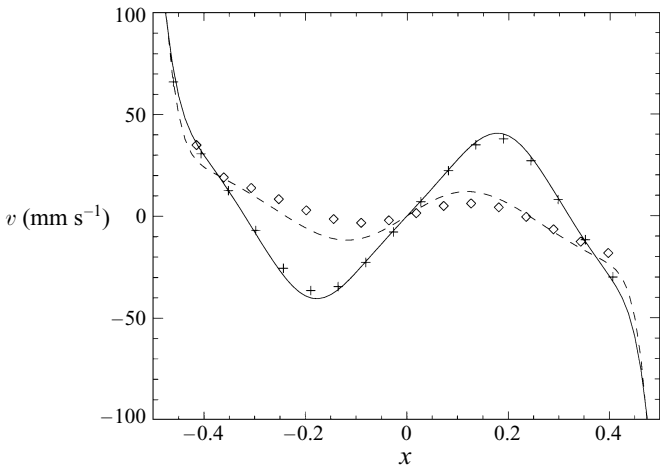


FIGURE 5. Velocity profiles $v(x)$ of the numerical two-vortex flow at $Re = 200$ (full line) and cat's eye flow at $Re = 240$ (dashed line). Velocity data measured by LDA at a distance $\Delta z = 50$ mm from the endwall are for: +, two vortex, $Re = 200$; ⋄, cat's eye, $Re = 240$.

Even though the internal cat's eye structure vanishes continuously on a further increase of the Reynolds number, giving way to a single vortex (an example is shown in figure 3*c*), we shall keep the notion of cat's eye flow and two-vortex flow to discern both types of base flow.

The agreement of the two-dimensional numerical and the quasi-two-dimensional experimental flow structures indicates that the combined effects of curvature of the moving sidewalls, endwall effects, and other imperfections (slight asymmetry in the experimental patterns) have a small influence on the flow pattern itself. In fact, the projections of the experimental quasi-two-dimensional streamline patterns do not change much over the major part of the cavity length (in the z-direction). Which of the two solutions is realized in the experiment, on the other hand, depends on the

https://doi.org/10.1017/S0022112096004727 Published online by Cambridge University Press

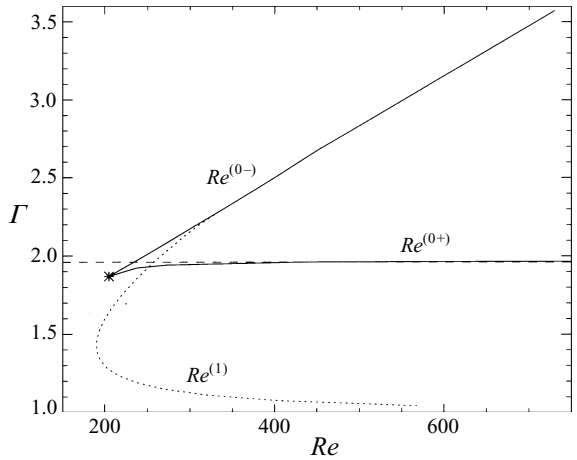


FIGURE 6. Region of non-uniqueness of the basic two-dimensional flow (full lines) bounded by $Re^{(0+)}$ (upper existence Reynolds number for the two-vortex state) and $Re^{(0-)}$ (lower existence Reynolds number for the cat's eye state) for symmetrical driving. The asterisk indicates the bifurcation point. The dotted line is the linear stability boundary $Re^{(1)}$ of the cat's eye flow. It intersects with $Re^{(0-)}$ at $\Gamma^* = 2.283$, $Re^* = 334$. The experimental aspect ratio $\Gamma = 1.96$ is shown as a dashed line.

time history and it may also depend on the imperfections, if the control parameters (here Re and Γ) are close to folds of the solution manifold, i.e. near catastrophe points. Here, the numerically determined lower transition Reynolds number $Re^{(0-)}$ is only 5% larger than the experimental Reynolds number for which the flow changes from cat's eye to two-vortex flow, while the numerical value $Re^{(0+)}$ is 184% larger than the experimentally observed transition Reynolds number. These differences may be explained by considering the shape of the region of non-uniqueness in the (Re, Γ)-plane obtained numerically. The area covered by the fold is shown as full lines in figure 6. For $\Gamma < 1.87 \pm 0.01$ the fold is absent and the solution depends smoothly on the Reynolds number. The bifurcation point of the catastrophe is located at the tip (asterisk in figure 6) $\Gamma_f = 1.87 \pm 0.01$ and $Re_f = 205 \pm 10$ of the triangular shaped region in figure 6. Thus the experimental aspect ratio is just slightly supercritical ($\Gamma > \Gamma_f$). The fold opens rapidly for $\Gamma > \Gamma_f$. Originating from (Re_f, Γ_f), the lower bound for which the cat's eye flow is found to exist ($Re^{(0-)}$) depends linearly on Γ at least up to $\Gamma = 3.5$. $Re^{(0-)}$ can be determined quite accurately. The fold corresponding to the upper Reynolds number limit for which the two-vortex flow exists ($Re^{(0+)}$) increases very rapidly with increasing Γ for $\Gamma > \Gamma_f$. Therefore, slight uncertainties in the experimental Γ-value result in an extremely large error for $Re^{(0+)}$. In fact, a much better agreement between the experimental and numerical values for $Re^{(0+)}$ and $Re^{(0-)}$ would have been obtained if we had defined the aspect ratio as $\Gamma = 1.91$ according to the minimum horizontal separation of the rotating cylinder surfaces. Numerical values for $Re^{(0+)}$ and $Re^{(0-)}$ are given in table 1.

4.2. *Neutral modes and slightly supercritical flow*

On a further increase of the Reynolds number the two-dimensional cat's eye flow becomes unstable to a stationary three-dimensional perturbation. The numerical results for aspect ratio $\Gamma = 1.96$ are presented first.

https://doi.org/10.1017/S0022112096004727 Published online by Cambridge University Press

Γ	$Re^{(0-)}$	Γ	$Re^{(0+)}$
1.87	205.0	1.87	205.0
1.96	234.3	1.92	237.5
2.01	250.0	1.94	272.5
2.17	300.0	1.96	427.5
2.50	400.0	1.98	> 1500
2.68	450.0		
3.57	730.0		

TABLE 1. Reynolds numbers $Re^{(0-)}$ and $Re^{(0+)}$ limiting the region of non-unique two-dimensional flow as function of the aspect ratio Γ for symmetrical driving.

The linear stability boundary of the cat's eye state as a function of the wavenumber is shown in figure 7. The neutral curve is very flat and a large wavenumber band becomes unstable. The critical value for the infinitely long system is $Re^{(1)}(\Gamma = 1.96) = 257.2$ at $k^{(1)} = 2.25$. The neutral disturbance mode is shown in figure 8. It consists of stationary rectangular convection cells, a single cell comprising half a wavelength in the z-direction. On the cell boundaries at constant z the w-component of the disturbance velocity vanishes. The disturbance flow on one such a cell boundary at, say $z = z_0 = 0$, is shown in figure 8(a). The disturbance velocity has a maximum at the centre of the cavity $x = y = 0$, the flow direction being approximately diagonal from the downstream cavity corner of one side ($x = \Gamma/2, y = -1/2$) to the downstream cavity corner of the other side ($x = -\Gamma/2, y = 1/2$). The corresponding backflow takes place at $z = z_0 \pm \lambda/2$. Halfway between the cell boundaries, at $z = z_0 \pm \lambda/4$, u and v vanish. Isolines of the w-component of the velocity at $z = \lambda/4$ are plotted in figure 8(b). Figure 8(c) shows the disturbance flow in a horizontal cut at $y = 0$. The flow in this plane takes the form of convection rolls. Therefore, the disturbance flow within a single cell can be imagined as a vortex for which the vorticity vector lies in the (x, y)-plane making an angle of approximately $-\pi/8$ with the positive y-axis. Superposing the basic cat's eye flow (figure 8d) with the critical disturbance flow of arbitrary amplitude results in the flow pattern shown in the figure 8(e) for $y = 0$.

Upon an increase of the Reynolds number, the experimental flow develops continuously out of the quasi-two-dimensional cat's eye flow to a strongly three-dimensional flow consisting of rectangular convection cells. The cells reveal themselves as planes at constant values of z which appear as sharp dark lines when viewed through the top lid. Thus the cell boundaries are easily detectable. One spatial period of the pattern consists of two cells. The z-extent of a single cell thus corresponds to one half of a fundamental wavelength.

The wavenumber realized in the experiment is restricted by the length of the cavity and it is locally influenced by the rigid end conditions at $z = \pm A/2$. Moreover, since the transition for symmetrical driving ($Re_1 = Re_2$) is experimentally found to be supercritical, the disturbance amplitudes are weak near the threshold. Therefore, the exact transition point is difficult to determine visually. At $Re^{(1)} = 260$ we find the first indication of a transition. At this Reynolds number a single cell appears approximately centred in the cavity at $z \approx 0$. In the rest of the cavity the flow is slightly three-dimensional, influenced by the front and rear boundaries, but no distinct cell character is visible there. The size of the single cell (half a wavelength) corresponds to a wavenumber $k^{(1)} = 2.2$. The single cell state is shown in figure 9 for $Re = 270$. The wavenumber of the corresponding periodic pattern would be $k = 2.13$.

https://doi.org/10.1017/S0022112096004727 Published online by Cambridge University Press

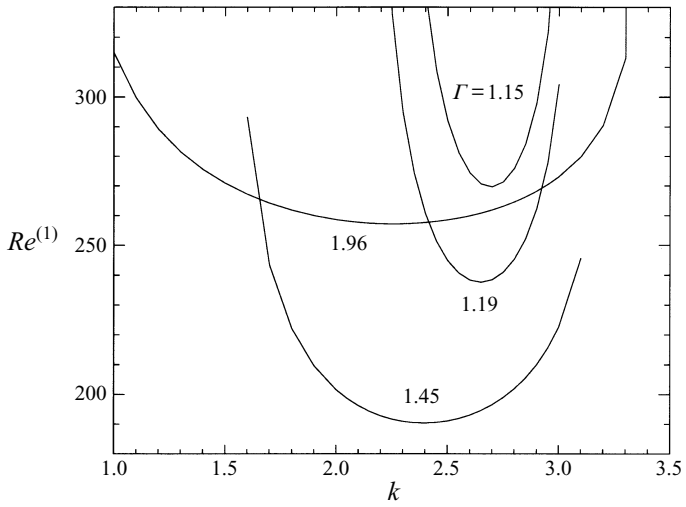


FIGURE 7. Linear stability curves for symmetrical driving: Re as function of the wavenumber k for different aspect ratios (as indicated by labels).

The convection cell is unambiguously discernable from the basic cat's eye state. Note that in the Taylor–Couette problem Taylor vortices also first appear in the middle between the endwalls (Alziary de Roquefort & Grillaud 1978).

The experimental threshold Reynolds number as well as the critical cell size are in agreement with the theoretical values of the cat's eye instability for symmetrical driving, $Re^{(1)} = 257.2$ and $k^{(1)} = 2.25$. Moreover, the flow structure (deviation from the cat's eye state) within the cell is very close to that of the neutral mode of the cat's eye instability (figure 8). These facts together with the supercritical nature of the bifurcation makes us conclude that the instability observed in the experiment corresponds to the numerically calculated cat's eye flow instability. It is a generic property of supercritical hydrodynamic bifurcations that the structure of the most unstable linear mode is conserved, although the amplitude and the phase may vary slowly in space for slightly supercritical conditions (Cross & Hohenberg 1993).

The dependence of the numerically determined neutral curves on the aspect ratio Γ is shown in figure 7 for $\Gamma = 1.15,\ 1.19,\ 1.45$, and 1.96. For high values of Γ, i.e. for a large separation of the moving boundaries, the neutral curves are very flat and a large wavenumber band opens up for $Re > Re^{(1)}(\Gamma)$. The neutral curves are not always symmetric with respect to $k^{(1)}(\Gamma)$ over the full range of k. For $\Gamma = 1.96$, for example, the neutral Reynolds number increases sharply near $k = 3.3$ and the neutral curve may eventually turn back. It may be noted that the fastest growing linear mode for $\Gamma = 1.96$ at $Re = 300$ has the wavenumber $k_{fastest} = 2.13 \pm 0.01$ (not shown) which is exactly the value detected experimentally for the slightly nonlinear one-cell state at $Re = 270$. If the aspect ratio decreases from $\Gamma = 1.96$ the k-bandwidth of the linearly unstable modes monotonically decreases and becomes quite narrow for $\Gamma = 1.15$. The neutral surface as a function of the parameters k and Γ has a minimum of $Re^{(1)} = 190.4$ at $\Gamma = 1.45 \pm 0.05$ and $k^{(1)} = 2.4 \pm 0.05$. The dependence of the neutral Reynolds number on the aspect ratio is shown in figure 10(a) for a fixed wavenumber $k = k^{(1)}(\Gamma = 1.96) = 2.25$. Also shown is the critical Reynolds number, i.e. the neutral Reynolds number minimized with respect to k. The critical wavenumber as a function of the aspect ratio is shown in figure 10(b). The critical Reynolds number

https://doi.org/10.1017/S0022112096004727 Published online by Cambridge University Press

curve exhibits a minimum. For large aspect ratios the critical Reynolds number increases slowly and the curve does not differ much from the neutral curve at fixed $k = k^{(1)}(\Gamma = 1.96) = 2.25$. A strong stabilization of the basic cat's eye flow occurs, however, when the aspect ratio approaches $\Gamma = 1$ from above.

4.3. *Fully developed three-dimensional flow*

On a quasi-steady increase of the Reynolds numbers the single stationary cell moves off the centre $z \approx 0$ and three more cells form simultaneously in the remainder of the cavity. They are clearly established for $Re \gtrsim 280$. The amplitude of the four cells grows with Re. A typical cellular pattern illuminated in a horizontal plane at $y = 0$ is shown in figure 11 for $Re = 750$. This type of steady pattern is very robust and exists for a wide range of Reynolds numbers. The wavenumber corresponding to the two inner cells is nearly constant over the investigated range of Reynolds numbers. It decreases slightly from the experimental critical value of $k = 2.20 \pm 0.05$ to $k = 2.10 \pm 0.05$ at $Re = 600$. This trend coincides with the wavenumber dependence of the fastest growing mode. By assigning a wavenumber to the two inner cells we anticipate that the experimental flow far from the boundaries would be periodic for asymptotically large values of Λ.

Two equivalent three-dimensional flow patterns are possible. For $Re_1 = Re_2$ the Navier-Stokes equations (3.1) are invariant under the transformation

$$(u, v, w, p, u_0, v_0, w_0, p_0, x, y, z, t) \quad \longrightarrow \quad (-u, -v, w, p, -u_0, -v_0, w_0, p_0, -x, -y, z, t) \tag{4.1}$$

for both the experimental ((3.2),(3.4)) and the numerical ((3.2),(3.3)) boundary conditions. The transformation corresponds to a rotation by π about the axis $x = y = 0$. While the basic state equations are invariant under this rotation, a periodic pattern like (3.6) experiences a phase shift in the z-direction by half a wavelength $\Delta z = \pm\pi/k$. Since this symmetry also holds for basic states that are perturbed by a nonlinear three-dimensional endwall-induced secondary flow, as in the current experiment, two different nonlinear three-dimensional convective states which differ by a phase shift of π are equally possible when $Re_1 = Re_2$. Both flow states are in fact realized experimentally. Which state prevails for long times $t \to \infty$ depends on the Reynolds number histories $Re_i(t)$. Note that this symmetry is removed when $Re_1 \neq Re_2$. In this case both states will differ from each other (see further below).

The associated wavenumber of the inner cells of the four-cell flow need not necessarily be the one that would be selected in the absence of endwalls. Moreover, as seen from the linear stability analysis, the k-band of linearly unstable modes gets larger as Re increases. Thus it should be possible to realize flow states with a different number of cells ($n \neq 4$). In fact, such states are found. In figure 12 a five-cell state viewed from the top is shown at $Re = 500$. Owing to the symmetry (4.1) two five-cell states exist, differing only by a 180° rotation around $x = y = 0$. Since the middle cell is separated symmetrically from the boundaries by two other cells, it is least influenced by the imperfect end conditions and therefore best suited to demonstrate the three-dimensional flow structure within a single cell. In figure 13(*a–c*) the projections of the streamlines within the light sheet are shown, taken at three different vertical planes within the middle cell, at the rear cell boundary ($z = -\lambda/4$), at the centre of the cell ($z = 0$), and at the front boundary ($z = \lambda/4$). At $z = 0$ the centre of the main vortex is located at the centreline $x = y = 0$ of the cavity. For $z = -\lambda/4$ the apparent vortex centre is located very close to the right-hand moving wall ($x = \Gamma/2$) and for $z = \lambda/4$ it is close to the left-hand moving

https://doi.org/10.1017/S0022112096004727 Published online by Cambridge University Press

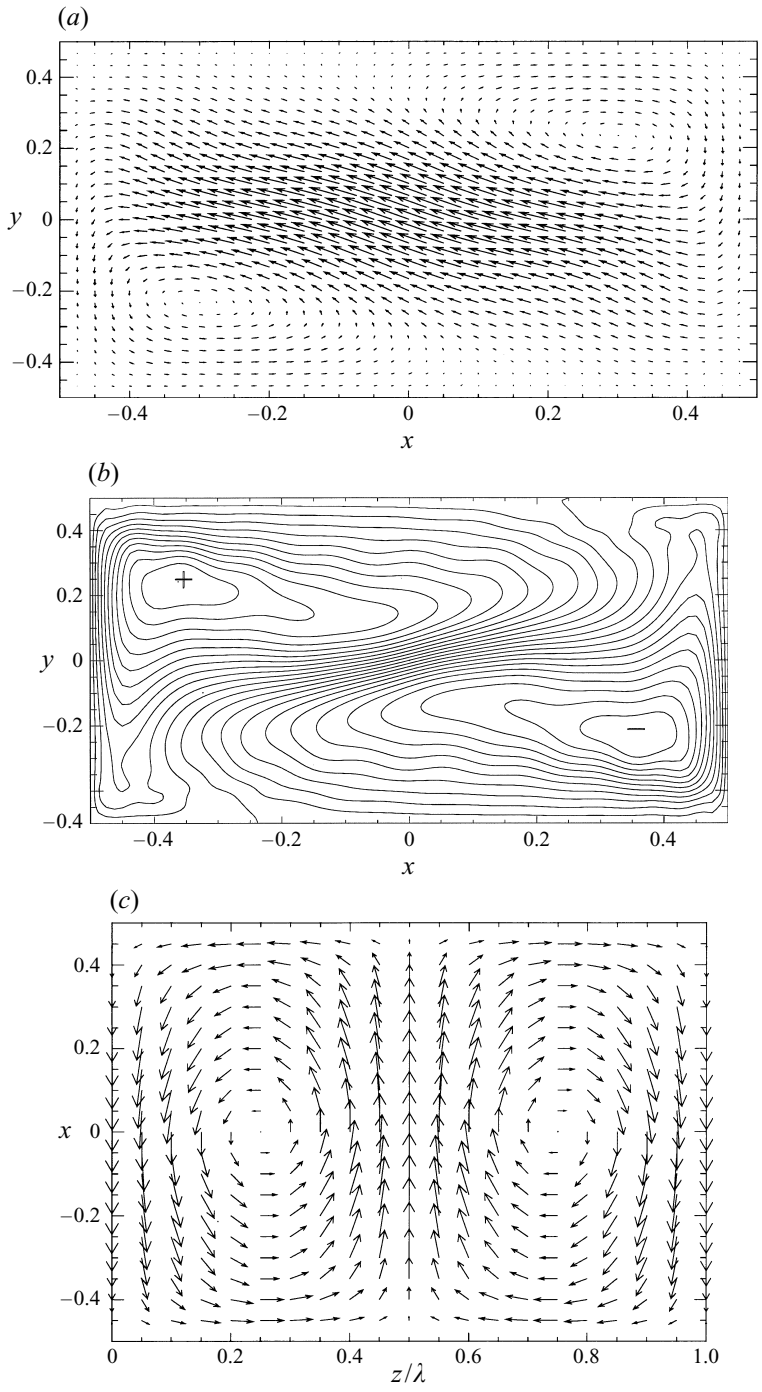


FIGURE 8. (*a*)–(*c*) For caption see facing page.

https://doi.org/10.1017/S0022112096004727 Published online by Cambridge University Press

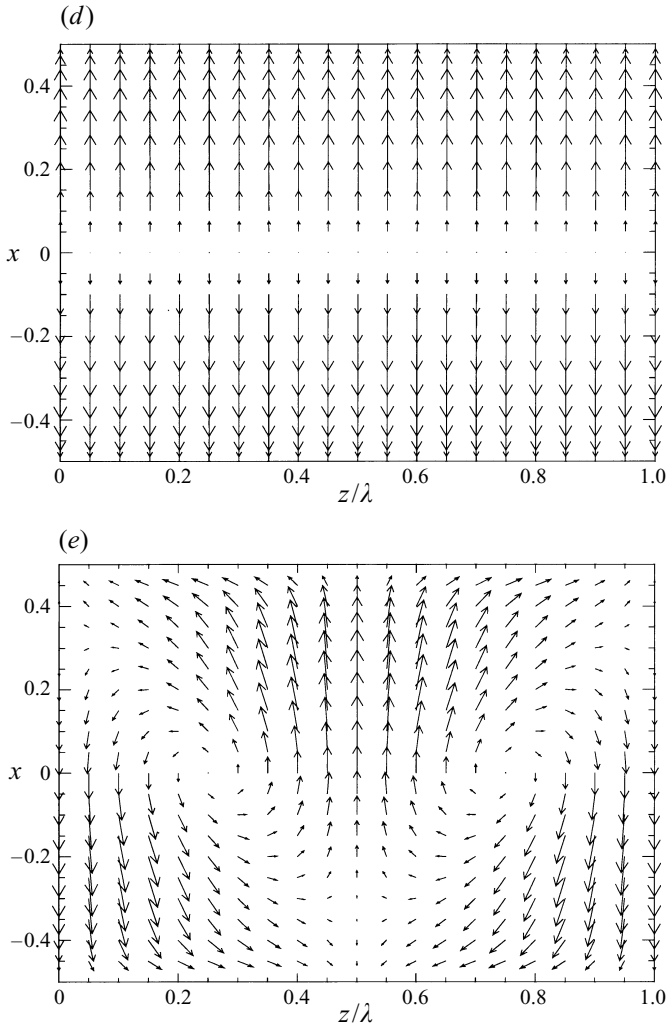


FIGURE 8. Neutral mode of the cat's eye base flow for $\Gamma = 1.96$, $k = k^{(1)} = 2.25$, and $Re^{(1)} = 257.2$ (symmetrical driving). (*a*) u, v in the (x, y)-plane at $z = 0$; (*b*) contour lines of w in the (x, y)-plane at $z = \lambda/4$; (*c*) u, w in the (x, z)-plane at $y = 0$; (*d*) basic cat's eye flow at $y = 0$; (*e*) superposition of the basic flow (*d*) with the disturbance (*c*) of arbitrary amplitude at $y = 0$. The x-axis is scaled by d.

wall ($x = -\Gamma/2$). For the second degenerate flow state the corresponding positions are obvious. The vortex centre thus makes a zigzag line in the ($y \approx 0$)-plane which is also visible in figures 11 and 12 as the bright diagonals within each cell. The diagonals correspond to regions of the nearly vanishing horizontal (x, y) velocities in figure 8(*e*). These flow characteristics equally apply to the supercritical flow with four cells.

The five-cell state is stable for a large range of Reynolds numbers. On decreasing Re in steps of $\Delta Re = 1$ and time intervals of 3 min, after every change the five-cell flow turned out to be stable down to $Re = 342 \pm 2$. Weaker ramps may have resulted in slightly smaller values of the minimum Reynolds number. However, weaker ramps become extremely time-consuming (the characteristic momentum diffusion time along

https://doi.org/10.1017/S0022112096004727 Published online by Cambridge University Press

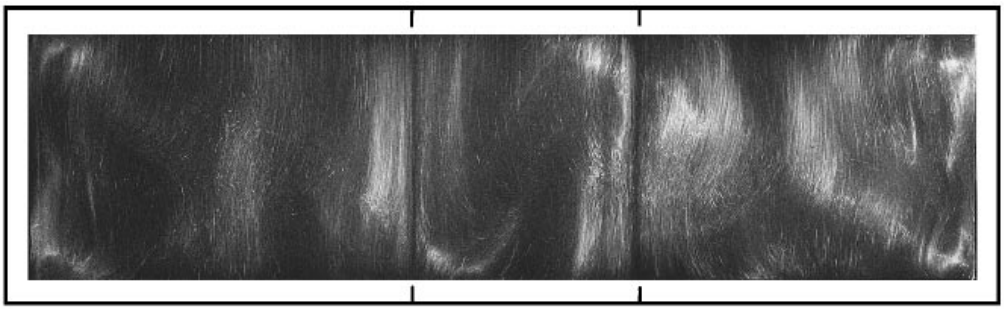


FIGURE 9. A single convection cell at $Re = 270$ slightly above the critical Reynolds number (symmetrical driving) illuminated by a light sheet at $y = 0$. The associated wavenumber is $k = 2.13$. The moving lid at the lower border moves towards the observer. The location of the cavity boundary according to $\Gamma = 1.96$ is given by the frame. The tic marks indicate the cell boundary.

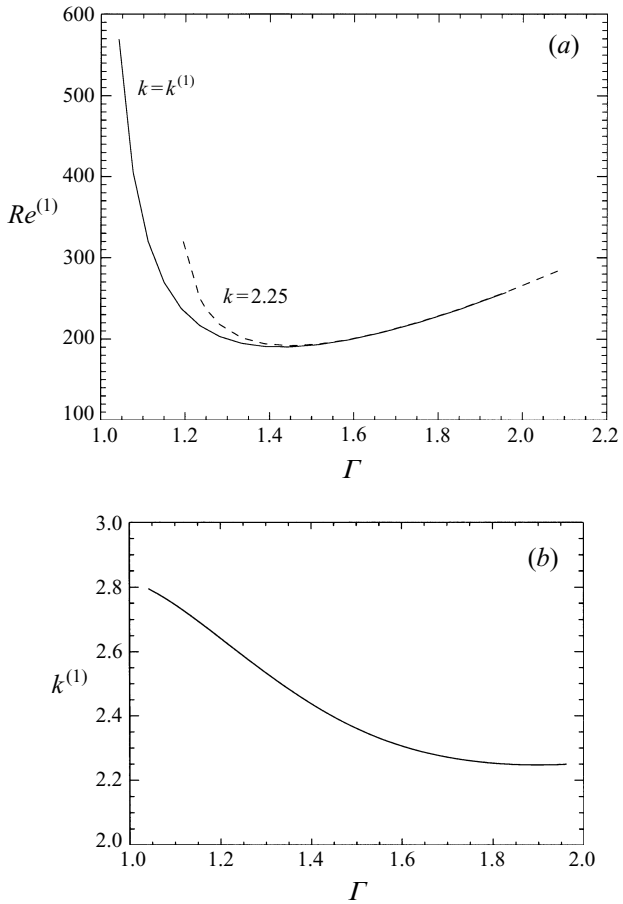


FIGURE 10. Critical curves as function of the aspect ratio Γ for the instability of cat's eye flow (symmetrical driving). (*a*) Neutral Reynolds number for fixed wavenumber $Re^{(1)}(k = 2.25)$ (dashed) and critical Reynolds number $Re^{(1)}(k = k^{(1)})$ (solid). (*b*) Critical wavenumber $k^{(1)}$.

https://doi.org/10.1017/S0022112096004727 Published online by Cambridge University Press

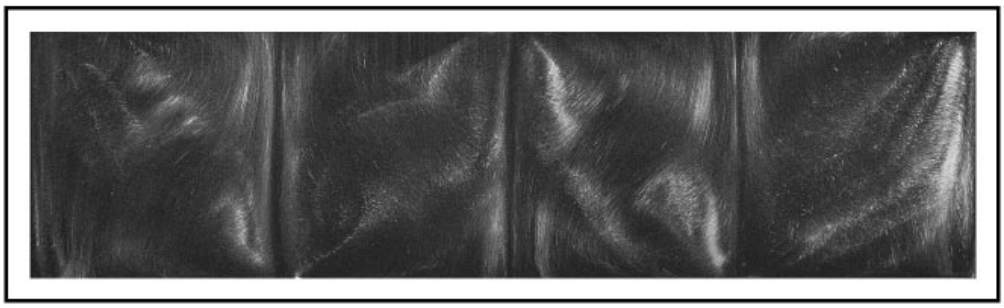


FIGURE 11. Fully developed four-cell state at $Re = 750$ for symmetrical driving. The moving lid at the bottom border moves towards the observer. The frame indicates the cross-section of the cavity. The light sheet at $y = 0$ entering from the right side causes a decay of the contrast to the left.

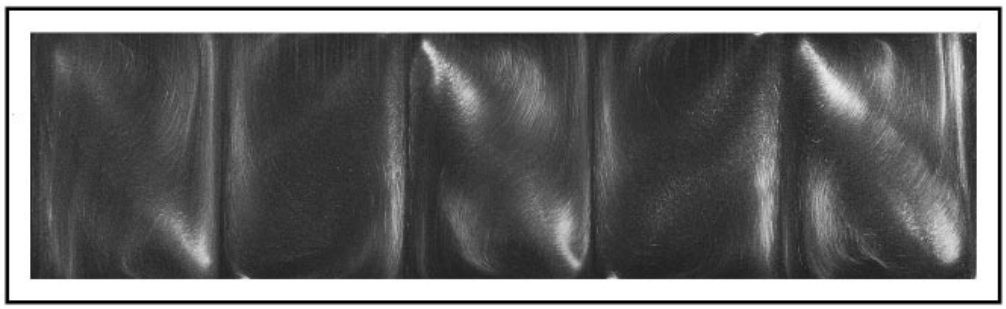


FIGURE 12. Five-cell state at $Re = 500$ for symmetrical driving. Conditions as in figure 11.

the cavity span is 25 min). The full existence range for five cell flow when $Re_1 \neq Re_2$ has not yet been explored.

4.4. *Linear instability of the two-vortex state*

The two-vortex state is experimentally found to be stable for $Re_1 = Re_2 < Re^{(0+)}$. It is not observed for $Re_1 = Re_2 > Re^{(0+)}$. As discussed above, this behaviour may be either due to an effective aspect ratio less than $\Gamma = 1.96$, or due to a premature transition. Therefore, no experimental information is available regarding the three-dimensional instability of the two-vortex flow for symmetrical driving. In particular, for aspect ratios larger than $\Gamma \gtrsim 2.0$ the two-vortex state exists up to high Reynolds numbers and its three-dimensional stability properties may become important. As will be shown below, the linear stability of this flow state is crucial, when the driving is not symmetric, i.e. for $Re_1 \neq Re_2$. The properties of the two-vortex instability will be presented, nevertheless, for $Re_1 = Re_2$ and $\Gamma = 1.96$. The linear stability analysis shows that the two-vortex state becomes unstable at $Re^{(2)}(\Gamma = 1.96) = 259.5$. The instability is stationary with a critical wavenumber of $k^{(2)} = 1.68$. This wavenumber would permit approximately $\Lambda k/2\pi \approx 1.75$ wavelengths to fit into the cavity. The neutral curve for $\Gamma = 1.96$ is shown in figure 14 as a function of the wavenumber. The velocity field of the neutral mode on a cell boundary, where w vanishes, is shown in figure 15. In this plane, the disturbance flow essentially consists of two counter-rotating vortices located in the middle of the cavity well separated from the moving lids. Obviously, the result of such a disturbance is to suppress one of the two basic co-rotating vortices and to enhance the other one. Owing to the periodicity in z, both vortices therefore become periodically varicose for supercritical driving, the

https://doi.org/10.1017/S0022112096004727 Published online by Cambridge University Press

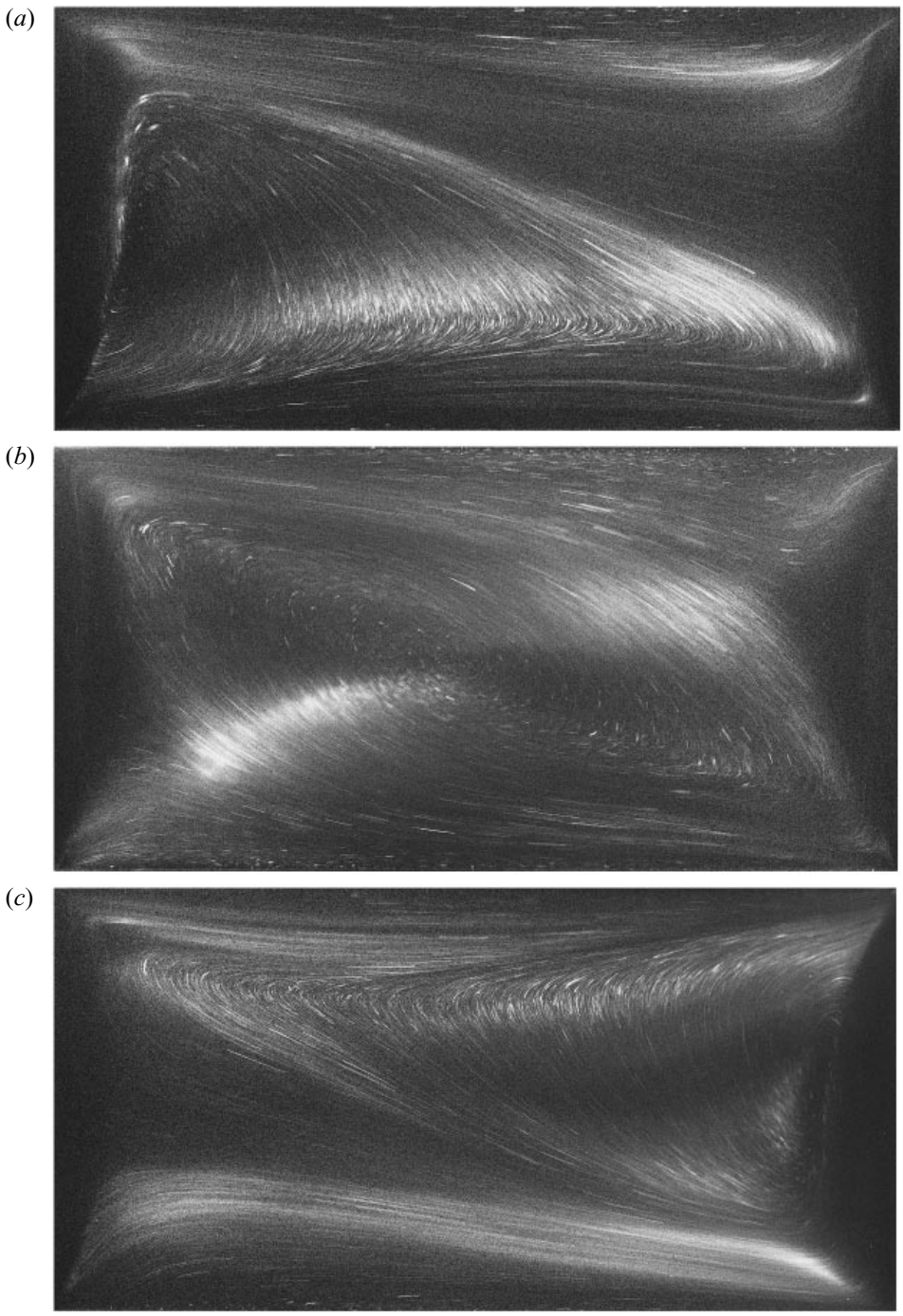


FIGURE 13. Cross-sections through the five-cell state at $Re = 500$ (symmetrical driving). (*a*) Cell boundary at $z = -\lambda/4$, (*b*) centre of the cell at $z = 0$, (*c*) cell boundary at $z = \lambda/4$. The flow is circulating clockwise.

https://doi.org/10.1017/S0022112096004727 Published online by Cambridge University Press

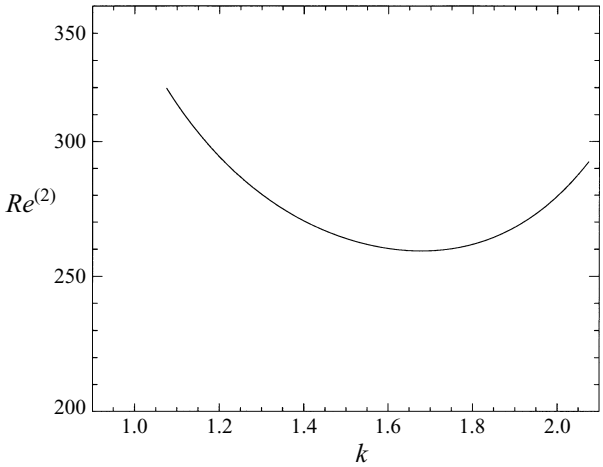


FIGURE 14. Linear stability curve $Re^{(2)}$ as a function of the wavenumber k for aspect ratio $\Gamma = 1.96$ and symmetrical driving ($Re_1 = Re_2$).

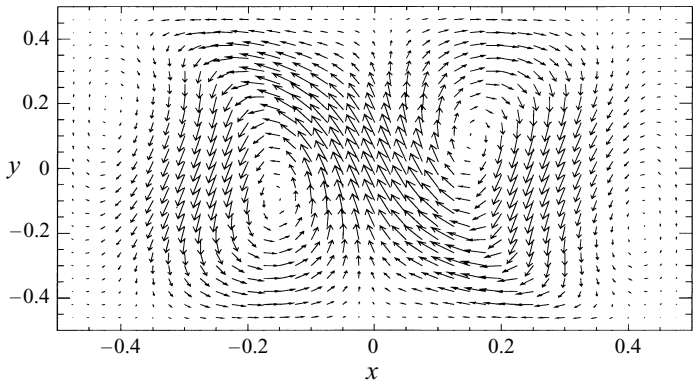


FIGURE 15. Neutral mode of the two-vortex flow state in the (x, y)-plane, where $w = 0$ ($Re_1 = Re_2$).

thickening and thinning of each being out of phase by π. Since the basic state and the neutral mode exhibit a stronger spatial variation than the respective fields of the cat's eye flow, a higher grid resolution is required to obtain reliable results. Here we have used 40 horizontal and 200 vertical grid points for the two-vortex instability calculations.

4.5. *Physical instability mechanisms*

To investigate the instability mechanisms that are responsible for the three-dimensional pattern formation described in the preceding sections the Reynolds–Orr energy equation for the rate of change of the kinetic energy

$$\partial_t E_{kin} = -D + \sum_{i=1}^{4} I_i \tag{4.2}$$

is evaluated for the most dangerous three-dimensional mode of the respective two-dimensional basic state. D is the rate of dissipation and the terms describing the

https://doi.org/10.1017/S0022112096004727 Published online by Cambridge University Press

interaction of the disturbance mode with the base flow are denoted by I_i:

$$D = \int_V (\nabla \times \boldsymbol{u})^2 \, \mathrm{d}V \ , \tag{4.3a}$$

$$\sum_{i=1}^{4} I_i = -\int_V \left\{ u^2 \frac{\partial u_0}{\partial x} + uw \frac{\partial u_0}{\partial y} + vu \frac{\partial v_0}{\partial x} + v^2 \frac{\partial v_0}{\partial y} \right\} \mathrm{d}V \ . \tag{4.3b}$$

The derivatives and integrals over the volume V are calculated from the numerically obtained basic and disturbance flow fields using second-order finite differences and Simpson's rule. The derivation of (4.2) and the evaluation of the integrals has been described by Wanschura *et al.* (1995).†

First, we discuss the instability of the cat's eye state. As a representative example we consider the case $\Gamma = 1.96$ and $k = k^{(1)} = 2.25$ for symmetrical driving ($Re = Re_1 = Re_2$). In figure 16 all terms in (4.3) contributing to the rate of change of energy are plotted as a function of Re for the mode with the largest growth rate. For small Reynolds number the balance is dominated by the dissipation D. The integral I_2 contributes most to the energy growth and becomes by far the dominant term when the Reynolds number is increased beyond the critical value. The integral I_2 describes the amplification of horizontal disturbance velocity u by vertical disturbance flow v perpendicular to the basic horizontal shear $\partial_y u_0$. The spatial distribution of the integrand of I_2 on the cell boundary at $z = 0$ is shown in figure 17. The amplification occurs in the centre of the cavity with a clear maximum at $x = y = 0$, the hyperbolic stagnation point of the cat's eye flow. Clearly, there is a considerable horizontal shear in this area (figure 3*b*). As can be seen from figure 8(*a*) the vertical disturbance flow near $x = y = 0$ is positive, transporting negative base-state x-momentum (u_0) from the lower part of the cavity to the centre, where the x-momentum of the disturbance (u) is also negative, thus amplifying it. An analogous explanation holds for the cell boundaries at $z = \pm\lambda/2$. The feedback is accomplished by the recirculation of the disturbance flow mainly in the (x, z)-plane as described in §4.2 above (see figure 8*c*).

The instability mechanism of the two-vortex state is mainly due to a similar process. The energy balance is shown in figure 18 for $Re_1 = Re_2$, $\Gamma = 1.96$, and $k = k^{(2)} = 1.68$. The instability is weaker than that of the cat's eye flow in the sense that the different contributions to the energy growth change only slowly with the Reynolds number. The reason is that the basic flow does not change its structure much with increasing Reynolds number. Here, the most destabilizing process is described by I_3. It corresponds to an amplification of the vertical disturbance velocity v by horizontal transport of vertical shear $\partial_x v_0$ due to a horizontal disturbance flow u. The basic state close to criticality shows three regions of vertical shear: both boundary layers near the moving walls, and the region between both basic vortices in the centre of the cavity. As can be seen from the space-resolved integrand of I_3 in the form of a double-peak in figure 19, the latter shear region provides the energy for the critical disturbance. The other destabilizing contribution, I_1, is the amplification of u due to the deceleration of the basic velocity u_0 near the separation point on the stationary walls downstream from the moving lids. The regions of amplification obtained from the combined space-resolved contribution of both I_1 and

† The total enstrophy $\int_V (\nabla \times \boldsymbol{u})^2 \, \mathrm{d}V$ differs from the total rate of dissipation $D = \int_V (\nabla \boldsymbol{u})^2 \, \mathrm{d}V$ by a surface integral that vanishes, if the velocity is zero everywhere on the boundary. As pointed out by a referee, more general conditions under which the enstrophy integral is equal to the total rate of dissipation have been discussed by Raynal (1996).

https://doi.org/10.1017/S0022112096004727 Published online by Cambridge University Press

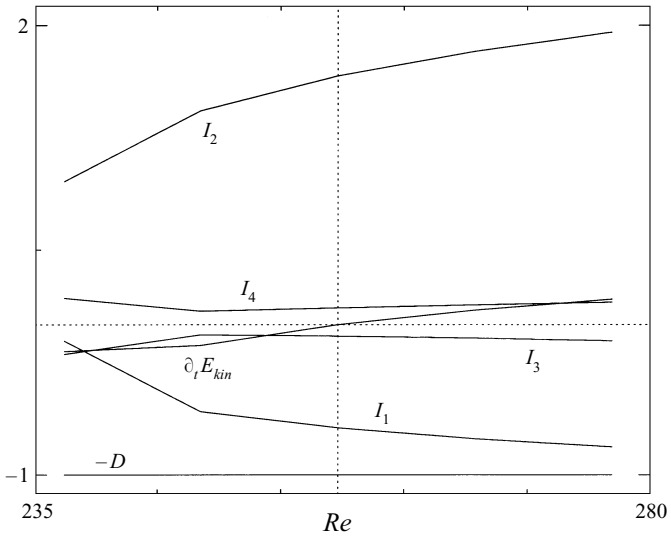


FIGURE 16. Energy balance of the most dangerous mode for the cat's eye state as a function of the Reynolds number for $\Gamma = 1.96$ and $k = 2.25$ (symmetrical driving). All terms are normalized by the dissipation D. The vertical dotted line indicates the critical Reynolds number.

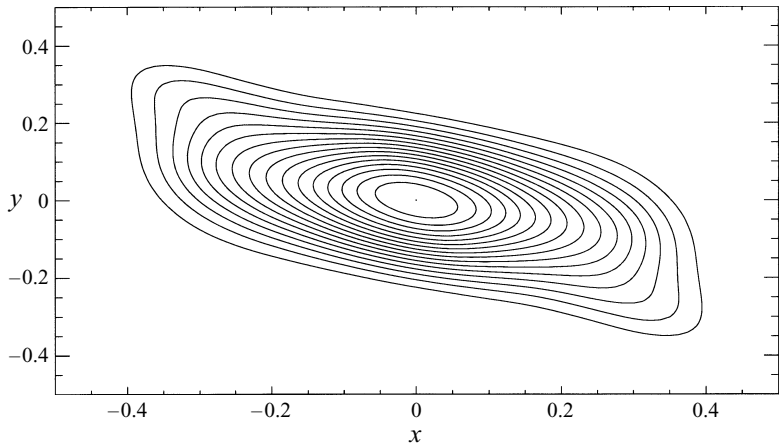


FIGURE 17. Isolines of the local (positive) energy transfer rate from the basic cat's eye state to the neutral disturbance due to the process I_2 shown at the cell boundary $z = 0$; $Re = Re^{(1)} = 257.2$, $k = k^{(1)} = 2.25$.

I_3 (not shown) are well localized close to both downstream separation points. Since the neutral mode is approximately a double roll (figure 15) the feedback required for an exponential growth essentially takes place in the same plane (constant z) contrary to the cat's eye instability.

4.6. $Re_1 \neq Re_2$

Considerations are now extended to the more general case of asymmetrical driving. Since the exchange of the Reynolds numbers $(Re_1, Re_2) \longrightarrow (Re_2, Re_1)$ corresponds to a rotation of the system by π around $x = y = 0$, all transition Reynolds numbers

https://doi.org/10.1017/S0022112096004727 Published online by Cambridge University Press

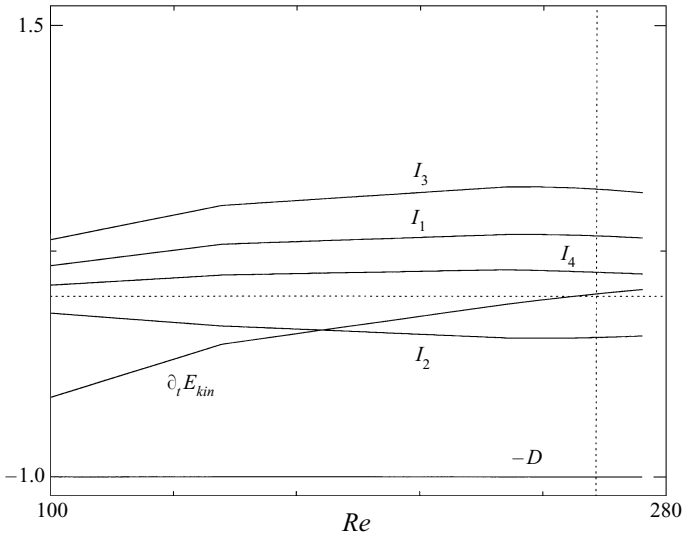


FIGURE 18. Energy balance of the most dangerous mode for the two-vortex state as function of the Reynolds number for $\Gamma = 1.96$ and $k = 1.68$ (symmetrical driving). All terms are normalized by the dissipation D. The vertical line indicates the critical Reynolds number.

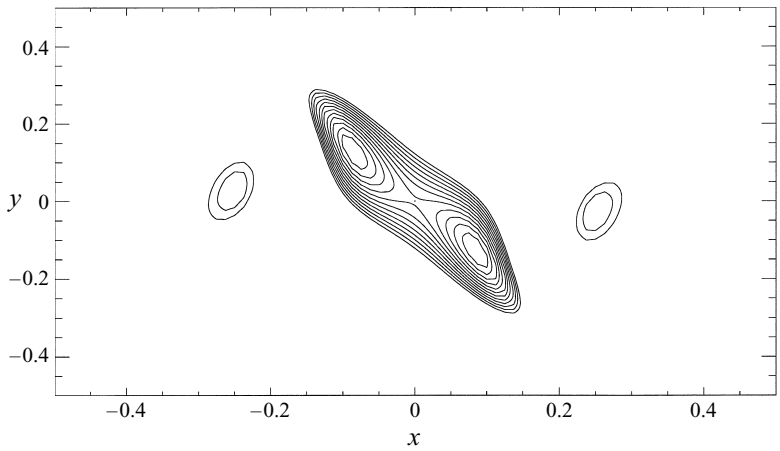


FIGURE 19. The local (positive) energy transfer rate from the basic two-vortex state to the neutral disturbance due to the process I_3 shown on the cell boundary ($z = 0$); $Re = Re^{(2)} = 253$, $k = k^{(2)} = 1.68$ (only the peak level lines are shown for clarity).

must be symmetrical with respect to the line $Re_1 = Re_2$. The full theoretical stability diagram for $\Gamma = 1.96$ is shown in figure 20.

Consider first the numerical results for the infinitely long system and $\Gamma = 1.96$. The curve limiting the existence range of the cat's eye flow ($Re_2^{(0-)}(Re_1)$), the dashed curve in figure 20, has been obtained by interpolating a representative set of transition points (table 2). The full curve in figure 20 is the neutral curve for the cat's eye flow calculated at a fixed wavenumber $k = k^{(1)} = 2.25$ (see also table 3).

In the parameter range shown this curve practically coincides with the critical curve ($k = k^{(1)}$) (compare figure 10*a*). Therefore, the minimization with respect to the wavenumber k of the Reynolds number varied was omitted. The validity of this

https://doi.org/10.1017/S0022112096004727 Published online by Cambridge University Press

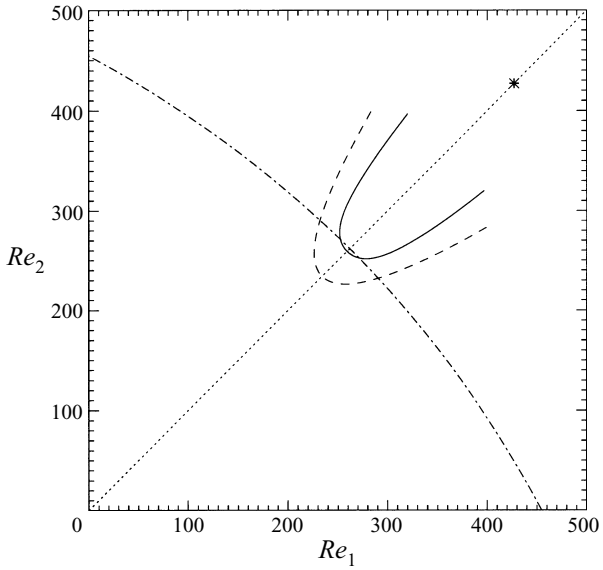


FIGURE 20. Transition boundaries for $Re_1 \neq Re_2$ and $\Gamma = 1.96$ (numerical results). Full line: linear stability boundary of the cat's eye flow. Dashed line: lower existence boundary of the cat's eye state. Asterisk: upper existence limit ($Re^{(0+)}$) of the two-vortex state for symmetrical driving. Dash-dotted line: linear stability boundary of the two-vortex flow.

approximation was checked for $Re_1 = 300$. The relative difference in $Re_2^{(1)}$ was only 0.02%.

The neutral stability boundary of the two-vortex state (dash-dotted line in figure 20; table 4) behaves differently. In particular, for sufficiently high asymmetry $\delta Re = Re_2 - Re_1$, this instability is the most dangerous one and the basic two-vortex flow state becomes three-dimensional on an increase of the Reynolds numbers before a transition to the cat's eye flow is possible. As before, the neutral curve was calculated for a constant wavenumber. Here we used $k = k^{(2)} = 1.68$. It was checked that the minimization with respect to k would at most yield a small correction of ± 3 in $Re_2^{(2)}$. Owing to the comparatively high grid resolution required for the linear stability analysis of the two-vortex state, only a few neutral Reynolds numbers have been computed (cf. table 4). The curve shown is an interpolation. The typical flow structures of both the basic two-vortex and the basic cat's eye flows do not change when δRe is increased moderately. Therefore, the same instability mechanisms as discussed in §4.5 for symmetrical driving hold for each type of base flow. While the cat's eye flow and its instability can be found close to the diagonal $Re_1 = Re_2$, it is interesting to note that the linear stability boundary reaches a finite value of $Re_2^{(2)} = 454$ when $Re_1 \to 0$ and vice versa. We have confirmed that even for $Re_1 = 0$ the neutral mode and the instability mechanism for the two-vortex flow instability at $Re_2 = 454$ is qualitatively the same as for symmetrical driving. In this case only the lower right peak of the double peak of the integrand of I_3 (figure 19) remains. It must be concluded that the two-vortex instability is not a result of an interaction of two vortices rather than a property of a single lid-driven vortex.

The theoretical values obtained for the infinitely long system are now compared with the experimental results. All experimental transition points have been obtained by keeping one Reynolds number fixed while varying the other one. In the following

https://doi.org/10.1017/S0022112096004727 Published online by Cambridge University Press

Re_1	$Re_2^{(0-)}$
400	284
360	261
320	243
280	229
234.3	234.3
229	280
243	320
261	360
284	400

TABLE 2. Lower existence boundary of the cat's eye flow state $Re_2^{(0-)}$ as a function of Re_1 for asymmetrical driving and $\Gamma = 1.96$.

Re_1	$Re_2^{(1)}$	Re_1	$Re_2^{(1)}$	Re_1	$Re_2^{(1)}$
257.2	257.2	305.0	259.2	355.0	288.3
260.0	255.8	310.0	261.5	360.0	291.8
265.0	253.2	315.0	263.9	365.0	295.5
270.0	252.0	320.0	266.5	370.0	299.2
275.0	251.6	325.0	269.2	375.0	303.0
280.0	251.9	330.0	272.1	380.0	306.9
285.0	252.7	335.0	275.1	385.0	310.9
290.0	253.9	340.0	278.3	390.0	314.9
295.0	255.4	345.0	281.5	395.0	319.0
300.0	257.2	350.0	284.8	400.0	323.3

TABLE 3. Neutral Reynolds numbers for the cat's eye flow instability $Re_2^{(1)}$ as a function of Re_1 at $k = 2.25$ and $\Gamma = 1.96$.

increasing or decreasing the Reynolds number means a change of either Re_1 or Re_2 while the other Reynolds number (Re_2 or Re_1) is kept constant. Critical values have been determined by variation of one Reynolds number in steps of $\Delta Re = 1$ and waiting for the lateral diffusion time $\tau_d \approx 2$ min between successive Reynolds number changes. For the pure two-dimensional flow transitions this time span is sufficient for a relaxation to the new state. But the cellular flow and the endwall effects are three-dimensional. The respective diffusive time scale in the z-direction is approximately $\tau_l = 25$ min. It was checked, however, that waiting for $\tau = \tau_d$ was sufficient, in most cases, to determine the final pattern. However, close to the supercritical instability for $Re_1 \approx Re_2$ longer time steps have been employed. Still, the uncertainty in the visually determined threshold values close to the symmetry axis in figure 21 is estimated to be of ± 7 on a Reynolds number scale. The error bar is smaller for larger asymmetry. For $(Re_1, Re_2) \gtrsim 350$ the instability is significantly hysteretic and the threshold values are reproducible up to the size of the symbols.

The filled circles in figure 21 represent the transition from the two-vortex flow to the cat's eye flow ($Re^{(0+)}$) when increasing the Reynolds number. The reverse transition back from cat's eye flow to two-vortex flow ($Re^{(0-)}$) during a decrease of the Reynolds number is indicated by open circles. In the cat's eye state, which is linearly stable for Reynolds numbers slightly beyond the two-dimensional transition curve, the flow is nearly two-dimensional over most parts of the cavity, even when the asymmetry δRe is large. As an experimental fact, the endwall imperfec-

https://doi.org/10.1017/S0022112096004727 Published online by Cambridge University Press

Re_1	$Re_2^{(2)}$
454.0	0.0
450.0	6.5
400.0	100.9
350.0	159.1
259.5	259.5
159.1	350.0
100.9	400.0
6.5	450.0
0.0	454.0

TABLE 4. Neutral Reynolds numbers for the two-vortex flow instability $Re_2^{(2)}$ as a function of Re_1 at $k = 1.68$ and $\Gamma = 1.96$.

tions are much stronger for the two-vortex state. The vortices of the two-vortex flow for large δRe are highly curved near both ends of the cavity at $z = \pm\Lambda/2$ even below the critical threshold. It is observed that the vortices of the two-vortex state are also wavy along their axes in the bulk, except when $Re_1 = Re_2$. Thus, we did not find a sharp transition from two-dimensional two-vortex flow to three-dimensional flow as expected along the dash-dotted theoretical curve in figure 20. This observation is interpreted as the consequence of a strongly imperfect bifurcation due to endwall effects. For that reason no experimental stability boundaries for the two-vortex state are given here. The two-vortex state may be more susceptible to three-dimensional endwall-induced perturbations due to the comparatively long wavelength of the critical mode. Endwall effects on the two-vortex state can only be avoided by using larger aspect ratios, $\Lambda > 10$, at least.

Once the cat's eye flow is established, it is stable for a certain range of Reynolds numbers. On increasing the Reynolds number beyond the line indicated by filled squares in figure 21 a transition to convective cells ($n = 4$) occurs. Since the symmetry (4.1) does not hold for asymmetrical driving, the degeneracy of the two possible patterns is removed. We observe that one of the supercritical states is uniquely selected at the onset of the cellular flow when $Re_2 > Re_1$. The other state is selected for $Re_1 > Re_2$. In the preferred state, the apparent vortex axis of the endwall cell originates from the corner made up of the endwall at, say $z = \Lambda/2$, and the fastest moving wall, i.e. the wall corresponding to the higher Reynolds number. If one endwall were at $z = 0$, the pattern shown in figure 8(*e*) would correspond to the prefered state, when $Re_2 > Re_1$. Once a four-cell state has been established, for say $Re_2 > Re_1$, the Reynolds numbers can be changed quasi-statically along a line $Re_1 + Re_2 = const.$ When crossing the line $Re_1 = Re_2$, however, the pattern which has evolved continuously will no longer be the favoured one. Finally, the transition to cat's eyes or supercritical two-vortex flow occurs on the other side of the stability diagram ($Re_1 > Re_2$). Except for a small region near this stability boundary (open squares in figure 21) the original four-cell pattern prevails. This is interpreted as a weak selection, i.e. the effective asymmetry between both possible patterns is small and both patterns have practically the same range of existence. Patterns with five cells were never found for quasi-static variations of the Reynolds numbers. No flows with a number of cells other than four or five were observed.

The transition point from cells to the cat's eye state during a decrease of Re

https://doi.org/10.1017/S0022112096004727 Published online by Cambridge University Press

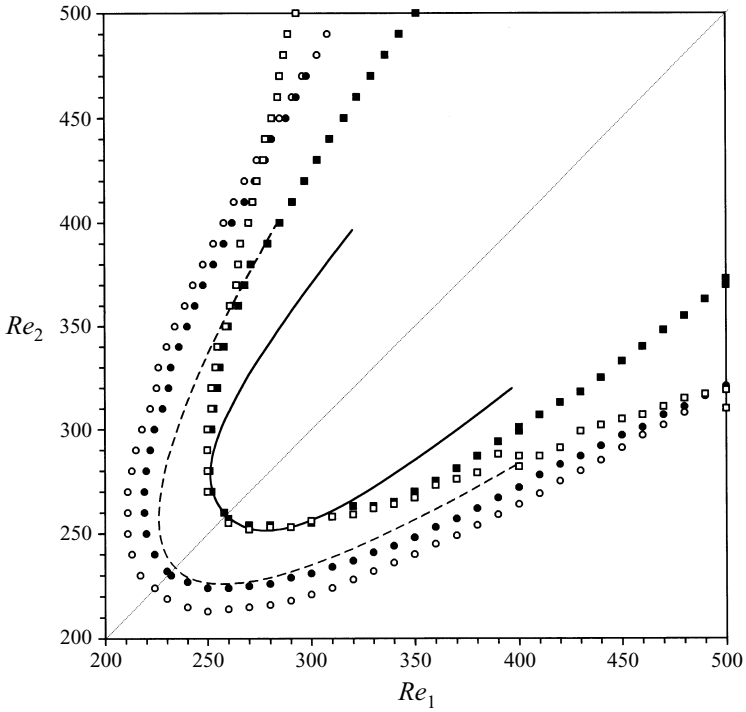


FIGURE 21. Transition boundaries for $Re_1 \neq Re_2$ and $\Gamma = 1.96$ (experimental results). •, two-vortex → cat's eye; ○ cat's eye → two-vortex; ■ cat's eye → three-dimensional cells, □ three-dimensional cells → cat's eye. The theoretical results are included as lines: – – –, cat's eye → two-vortex; ——, linear instability boundary of the cat's eye flow.

is indicated by open squares in figure 21. With increasing asymmetry (δRe) the transition gets more and more hysteretic. It is anticipated that the instability is strictly supercritical only when $Re_1 = Re_2$. For Reynolds numbers $Re \gtrsim 470$ the line indicated by open squares intersects the curves of transition between supercritical two-vortex and cat's eye flow. Thus, if one Reynolds number is larger than $Re \gtrsim 470$, the cellular pattern breaks down on a decrease of Re to a supercritical two-vortex flow which is already three-dimensional.

The lines in figure 21 represent the theoretical curves. Good agreement with the experimental data is obtained for the three-dimensional instability of cat's eye flow at symmetrical driving (low Re). For high Reynolds numbers cellular flow is found to exist for a larger range of Reynolds numbers than predicted by the linear stability analysis. This discrepancy is not a contradiction, however, because the transition is hysteretic. If the hysteresis for $Re_1 \neq Re_2$ is a property of the ideal infinitely long system, the presence of endwalls and other imperfections may cause finite-amplitude perturbations so that cells can appear subcritically prior to the linear stability limit.

The difference of $O(20)$ on a Reynolds number scale between the numerically predicted existence range of cat's eye flow (dashed line in figure 22) and the experimentally determined curve (open circles) has been interpreted in terms of the sensitive dependence of these curves on the aspect ratio (§4.1). Since the Reynolds numbers have been controlled to within 1%, the remaining asymmetry in the experimental data points is most likely to be due to minute aspect ratio changes along the z-direction.

https://doi.org/10.1017/S0022112096004727 Published online by Cambridge University Press

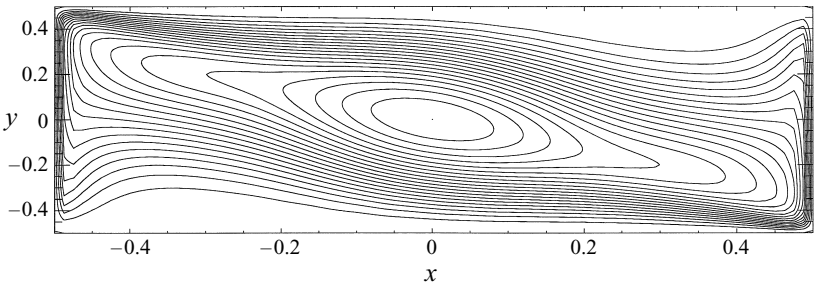


FIGURE 22. Two-dimensional cat's eye flow for $\Gamma = 3.3$ for symmetrical driving at $Re = 800$. The flow is linearly unstable. The x-axis is scaled by d.

5. Discussion

First, the results obtained for the instability of the two-vortex state are compared with existing numerical results for the one-sided lid-driven cavity. Since the two-vortex instability mechanism is not altered for one-sided driving ($Re_1 = 0$), the instability is independent of a second vortex in the cavity. This result appears to be in qualitative agreement with that of Ramanan & Homsy (1994) for $Re_1 = 0$ and $\Gamma = 1$ who found a critical value of $Re_2^{(2)} \approx 600$ at $k \approx 2$ for a resolution of 64×64 finite difference points. In fact, the location and the shape of the contour lines of the sum of the integrands of the energy integrals I_1 and I_3 for $Re_1 = 0$ and $\Gamma = 1.96$ are nearly the same as those in figure 8(a) of Ramanan & Homsy (1994). During test calculations for $\Gamma = 1$ we obtained a similar result using a low resolution of 40×15 grid points. However, the stationary threshold value did increase with the resolution and for 200×40 finite-difference/collocation points we obtained $Re_2^{(2)}(k = 2) > 2500$. We must conclude that the result of Ramanan & Homsy (1994) is not accurate, because the stability limit for the one-sided lid-driven cavity flow with $\Gamma = 1$ is highly grid-dependent. Obviously, the critical mode is significantly stabilized by the rigid wall being close to the vortex for $\Gamma = 1$. This result is compatible with the existing experimental data (Koseff & Street 1984). The typical Taylor–Görtler-like vortices found in experiments and numerical simulations of the classical cavity problem have a much smaller wavelength than the critical mode of the two-vortex flow for $Re_1 = 0$ and $\Gamma = 1.96$ which is a large-scale mode with a wavelength $\lambda = 3.7$.

Next, we turn to the two-dimensional transition from the two-vortex to the cat's eye state on a decrease of Γ. For $\Gamma = 1.96$ the diameter D of a single vortex ($Re_2 = 0$), defined as the distance along $y = 0$ from $x = -\Gamma/2$ to the separating streamline of the vortex, decreases monotonical from $D \approx 1.4$ for creeping flow through $D = 1.22$ at $Re_1 = 100$ to the constant value $D = 0.94$ in the range $500 < Re_1 < 10^3$. For $Re_1 = 10^3$ the vorticity is already nearly constant in the vortex core. Therefore, the vortices generated by both moving walls at high Reynolds numbers individually have the tendency to attain a nearly unit aspect ratio. We find that the flow with two square vortices exists for high Re and cavity aspect ratios larger than $\Gamma \gtrsim 2$ (see figure 6). There is evidence that the Reynolds number $Re^{(0+)}(\Gamma)$ describing the upper existence limit for the two-vortex state diverges for $\Gamma \uparrow 2$. This is about the aspect ratio for which the separating streamlines of both vortices would touch on a decrease of Γ leading to a two-dimensional abrupt structural change of the flow for $Re > Re_f$. In the present experiment this transition is a dynamic process taking $O(1)$ s. It may be viewed as a partial vortex merging in a cavity. An analogy to the merging of vortex patches in unbounded ideal flow (Melander, Zabusky & McWilliams 1988), however,

https://doi.org/10.1017/S0022112096004727 Published online by Cambridge University Press

cannot be directly established mainly due to the different boundary conditions in both cases.

Based on a scaling consideration Pan & Acrivos (1967) argued that the extent in the x-direction of the primary vortex driven by a single moving wall in a cavity of infinite depth ($\Gamma \to \infty$) should scale like $Re^{1/2}$ for high Re. Such a behaviour is not observed for the two-vortex state. If, moreover, this scaling were to hold for the merged cat's eye state, the lower existence curve $Re^{(0-)}$ for the cat's eye state should scale like $\Gamma \sim (Re^{(0-)})^{1/2}$. This is not the case. Instead, a linear dependence $Re^{(0-)} \sim \Gamma$ is found.

The linear dependence of the lower existence curve for the cat's eye state on the Reynolds number can be explained as follows. In the limit of high Reynolds numbers the fluid in the conventional boundary layer on to the moving wall at $x = \Gamma/2$ is accelerated and released into the cavity in the form of a wall jet along the stationary downstream wall at $y = -1/2$. The boundary layer thickness Δ of a wall jet scales like $\Delta \sim (x/Re)^{3/4}$ (Batchelor 1967), where x measures the distance from the origin of the wall jet. In order that a recirculating flow occupying the whole cavity is sustained, the wall jet must be entrained by the boundary layer of the moving wall on the opposite side ($x = -\Gamma/2$). Here the jet, which has slowed down, is again accelerated to form another wall jet in the opposite direction and on the opposite stationary wall at $y = 1/2$. For this process to be effective it is required that the wall jets remain confined sufficiently close to the rigid walls, i.e. the boundary layer thickness must be less than a value $\Delta \leqslant O(1)$, since the cavity height is $O(1)$. The limiting case is thus given by $\Delta(x = \Gamma) \sim (\Gamma/Re)^{3/4} = O(1)$. It follows that the limiting aspect ratio must depend linearly on Re, i.e. $\Gamma \sim Re$. This is the observed dependence. The numerical results lead us to anticipate that the cat's eye flow will persist for all aspect ratios in the limit of high Reynolds numbers and symmetrical driving. We conclude that the flow is not unique in the limit of high Reynolds numbers $Re_1 = Re_2 \to \infty$ when the aspect ratio is larger than a critical value Γ_0 which was estimated above to be $\Gamma_0 \approx 2.0$. An example for the cat's eye flow (three-dimensionally unstable) in a large aspect ratio cavity ($\Gamma = 3.3$) is given in figure 22 for $Re_1 = Re_2 = 800$. The wall jets are clearly visible.

Finally, we consider the cat's eye flow instability. At unit aspect ratio $\Gamma = 1$ and symmetrical driving, the centre of the vortex far away from the endwalls has circular streamlines. This flow is linearly stable for the Reynolds numbers considered (see figure 10*a*). When for high Reynolds numbers ($Re > Re_f$) and symmetrical driving the aspect ratio increases from unity, the cat's eye flow develops continuously from the square cavity flow. The shapes of the streamlines in the interior become increasingly elliptic and the flow is rapidly destabilized (figures 6, 10*a*) even before it develops the typical cat's eye shape. Based on the following observations we conclude that the instability of the cat's eye flow is a manifestation of the elliptic instability (Pierrehumbert 1986; Bayly 1986; Landman & Saffman 1987; Waleffe 1990). First, both instabilities are stationary ($\omega^{(1)} = 0$) in the frame moving with the elliptic vortex. Second, the energy transfer rate from the base flow to the disturbance is largest at the centre of the vortex (cf. figure 17). There the flow is a superposition of a solid-body rotation and a straining motion, for which the stream function can be written locally as

$$\psi(x, y) = \tfrac{1}{2}\left((\gamma - \epsilon)\, x^2 + (\gamma + \epsilon)\, y^2\right) , \tag{5.1}$$

where $\gamma > 0$ is the rotation rate, $\epsilon > 0$ is the rate of strain, and the coordinate system is slightly rotated (cf. figure 3*b*). A cat's eye structure corresponds to $\epsilon > \gamma$, indicating

https://doi.org/10.1017/S0022112096004727 Published online by Cambridge University Press

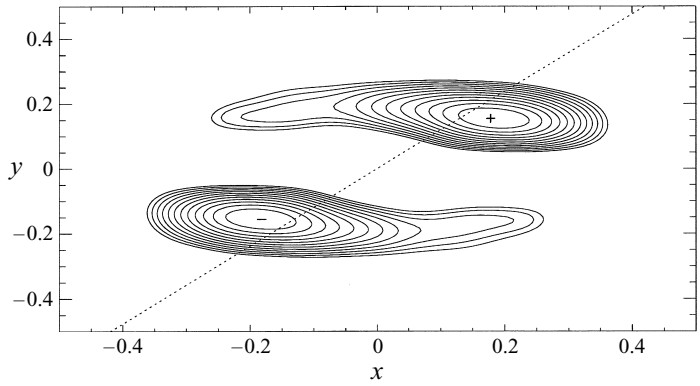


FIGURE 23. z-component of the vorticity (ω_z) in the plane $z = \lambda$ (cf. figure 8). The dotted line is the strain direction at the centre of the cavity.

the dominating straining motion in the centre $x = y = 0$ for the cat's eye flow. Third, a striking similarity is the sharp stabilization of the present two-dimensional flow when $\Gamma \to 1$, and the stability of the unbounded elliptic vortex when the eccentricity is zero. Fourth, the structure of the vorticity of both neutral modes is similar in both cases. For the elliptic instability the z-component of the vorticity of the neutral mode has extrema along the stretching plane which makes a 45° angle with respect to the x- and y-axes ($y = x$ in (5.1)). The same behaviour is found for the highly strained basic cat's eye flow at $\Gamma = 1.96$ for which the direction of the strain is given by the dotted line in figure 3(b). As can be seen in figure 23 the strain direction nearly intersects with the extrema of the z-component of the vorticity of the critical mode. Owing to the present base flow structure (wall jets) the extrema are slightly displaced downstream. The vorticity distribution is very close to those given by Pierrehumbert (1986) and Waleffe (1990). Pierrehumbert (1986) showed that the instability in ideal fluids is universal, acting on arbitrary small length scales. Here we find that $k^{(1)} = O(1)$ in units of the cavity height h, in qualitative agreement with the viscous wavelength cut-off found by Landman & Saffman (1987) for viscous elliptic eddies.

In addition to the similarities of the linear properties of both instabilities, the steady highly nonlinear three-dimensional cellular cavity flow exhibits characteristics similar to the transitional flow in the decay of an elliptic vortex to turbulence. During the early stages of the decay of an elliptic vortex Lundgren & Mansour (1996) observed that the vorticity field gets greatly distorted into sheet-like structures. These sheet-like regions of concentrated vorticity are clearly visible in figure 13(a–c) as strongly curved lines of projected particles traces.

Flows with elliptic streamlines evolve smoothly to hyperbolic stagnation point flow when ϵ becomes larger than γ. For that reason the observed destabilization of the strain-dominated cat's eye flow in the cavity ($\epsilon > \gamma$) can also be considered a viscous realization of the instability of hyperbolic stagnation point flow in ideal fluids (Lifshitz & Hameiri 1991).

The two-dimensional cat's eye flow becomes unstable throughout its full existence range (for all Re) when $\Gamma > \Gamma^* = 2.283 \pm 0.003$, which is the aspect ratio for which the three-dimensional instability curve crosses the lower existence curve for the cat's eye state ($Re^{(0-)*} = 334 \pm 2.2$) (figure 6). This property is not surprising, since the base flow for large aspect ratios will be close to a plane shear flow in which two-dimensional equilibria are usually unstable. The limit of large Γ may establish a

https://doi.org/10.1017/S0022112096004727 Published online by Cambridge University Press

correspondence between cat's eye flow instability and the three-dimensional instability of two-dimensional equilibria in plane shear flows.

In conclusion, we have shown that the flow in rectangular two-sided lid-driven cavities with non-square cross-section exhibits different instabilities. The cellular flow instability of the basic cat's eye flow at low Reynolds numbers is not present in one-sided lid-driven cavities. This type of flow offers the opportunity to study the elliptic flow instability in detail, because the underlying base flow is stationary. This is the major advantage of the present geometry. Previous experimental investigations of the elliptic instability typically considered the spin-down of the flow in cylinders with elliptical cross-section suddenly stopped from rigid-body rotation (see e.g. Gledzer & Ponomarev 1992), which has the disadvantage of being transient. The present results, moreover, may provide a key for the understanding of three-dimensional shear-driven cavity flows as well as lid-driven cavity flows in other geometries.

The authors are very grateful to S. Albensoeder and M. Kamp for their assistance in setting up the experiment. We also acknowledge constructive comments of the referees. This work was supported by Deutsche Forschungsgemeinschaft under grant number Ku896/5-1.

REFERENCES

Aidun, C. K., Triantafillopoulos, N. G. & Benson, J. D. 1991 Global stability of a lid-driven cavity with throughflow: flow visualization studies. *Phys. Fluids* A **3**, 2081.

Alziary de Roquefort, T. & Grillaud G. 1978 Computation of Taylor vortex flow by a transient implicit method. *Computers Fluids* **6**, 259.

Amon, C. H. & Patera, A. T. 1989 Numerical calculation of stable three-dimensional tertiary states in grooved channel flow. *Phys. Fluids* A **1**, 2005.

Batchelor, G. K. 1956 On steady laminar flow with closed streamlines at large Reynolds number. *J. Fluid Mech.* **1**, 177.

Batchelor, G. K. 1967 *An Introduction to Fluid Dynamics*. Cambridge University Press.

Bayly, B. J. 1986 Three-dimensional instability of elliptical flow. *Phys. Rev. Lett*. **57**, 2160.

Bayly, B. J., Orszag, S. A. & Herbert, Th. 1988 Instability mechanisms in shear flow transition. *Ann. Rev. Fluid Mech.* **20**, 359.

Bödewaldt, U. T. 1940 Die Drehströmung über festem Grunde. *Z. Angew. Math. Mech.* **20**, 241.

Burggraf, O. R. 1966 Analytical and numerical studies of the structure of steady separated flows. *J. Fluid Mech.* **24**, 113.

Cross, M. C. & Hohenberg, P. C. 1993 Pattern formation outside of equilibrium. *Rev. Mod. Phys.* **65**, 851.

Deville, M., Lê, T.-H. & Morchoisne, Y. (Eds.) 1992 *Numerical Simulation of 3-D Incompressible Unsteady Viscous Laminar Flows*. Notes on Numerical Fluid Mechanics, vol. 36. Vieweg.

Di Prima, R. C. & Swinney, H. L. 1981 Instabilities and transition in flow between concentric rotating cylinders. In *Hydrodynamic Instabilities and the Transition to Turbulence* (ed. H. L. Swinney & J. P. Gollub). Topics in Applied Physics vol. 45, p. 139. Springer.

Freitas, C. J., Street, R. L., Findikakis, A. N. & Koseff, R. J. 1985 Numerical simulation of three-dimensional flow in a cavity. *Intl J. Numer. Meth. Fluids* **5**, 561.

Ghaddar, N. K., Korczak, K. Z., Mikic, B. B. & Patera, A. T. 1986 Numerical investigation of incompressible flow in grooved channels. Part 1. Stability of self-sustained oscillations. *J. Fluid Mech.* **163**, 99.

Gledzer, E. B. & Ponomarev, V. M. 1992 Instability of bounded flows with elliptical streamlines. *J. Fluid Mech.* **240**, 1.

Goodrich, J. W., Gustafson, K. & Halasi, K. 1990 Hopf bifurcation in the driven cavity. *J. Comput. Phys.* **90**, 219.

https://doi.org/10.1017/S0022112096004727 Published online by Cambridge University Press

Jana, S. C., Metcalfe, G. & Ottino, J. M. 1994 Experimental and numerical studies of mixing in complex Stokes flow: the vortex mixing flow and multicellular cavity flow. *J. Fluid Mech.* **269**, 199.

Koplik, J. & Banavar, J. R. 1995 Corner flow in the sliding plate problem. *Phys. Fluids* **7**, 3118.

Koseff, R. J. & Street, R. L. 1984 The lid-driven cavity: a synthesis of qualitative and quantitative observations. *Trans. ASME: J. Fluids Engng* **106**, 390.

Koseff, J. R., Street, R. L., Gresho, P. M., Upson, C. D., Humphrey, J. A. C. & To, W.-M. 1983 A three-dimensional lid-driven cavity flow: experiment and simulation. *Proc. 3rd Intl Conf. on Numerical Methods in Laminar and Turbulent Flow* (ed. C. Taylor). Pineridge Press.

Landman, M. J. & Saffman, P. G. 1987 The three-dimensional instability of strained vortices in a viscous fluid. *Phys. Fluids* **30**, 2339.

Leong, C. W. & Ottino, J. M. 1989 Experiments on mixing due to chaotic advection in a cavity. *J. Fluid Mech.* **209**, 463.

Lifshitz, A. & Hameiri, E. 1991 Local stability conditions in fluid dynamics. *Phys. Fluids* A **3**, 2644.

Lundgren, T. S. & Mansour, N. N. 1996 Transition to turbulence in an elliptic vortex. *J. Fluid Mech.* **307**, 43.

Maull, D. J. & East, L. F. 1963 Three-dimensional flow in cavities. *J. Fluid Mech.* **16**, 620.

Melander, M. V., Zabusky, N. J. & McWilliams, J. C. 1988 Symmetric vortex merger in two dimensions: causes and conditions. *J. Fluid Mech.* **195**, 303.

Moffatt, H. K. 1964 Viscous and resistive eddies near a sharp corner. *J. Fluid Mech.* **18**, 1.

Neary, M. D. & Stephanoff, D. 1987 Shear-layer-driven transition in a rectangular cavity. *Phys. Fluids* **30**, 2936.

Pan, F. & Acrivos, A. 1967 Steady flows in rectangular cavities. *J. Fluid Mech.* **28**, 643.

Pierrehumbert, R. T. 1986 Universal short-wave instability of two-dimensional eddies in an inviscid fluid. *Phys. Rev. Lett.* **57**, 2157.

Prasad A. K. & Koseff, J. R. 1989 Reynolds number and end-wall effects on a lid-driven cavity flow. *Phys. Fluids* A **1**, 208.

Ramanan, N. & Homsy, G. M. 1994 Linear stability of lid-driven cavity flow. *Phys. Fluids* **6**, 2690.

Raynal, F. 1996 Exact relation between spatial mean enstrophy and dissipation in confined incompressible flows. *Phys. Fluids* **8**, 2242.

Rhee, H. S., Koseff, J. R. & Street, R. L. 1984 Flow visualization of recirculating flow by rheoscopic liquid and liquid crystal technique. *Exps. Fluids* **2**, 57.

Shen, J. 1991 Hopf bifurcation of the unsteady regularized driven cavity flow. *J. Comput. Phys.* **95**, 228.

Vahl Davis, G. de & Mallinson, G. D. 1976 An evaluation of upwind and central difference approximations by a study of recirculating flow. *Computers Fluids* **4**, 29.

Waleffe, F. 1990 On the three-dimensional instability of strained vortices. *Phys. Fluids* A **2**, 76.

Wanschura, M., Shevtsova, V. M., Kuhlmann, H. C. & Rath, H. J. 1995 Convective instability mechanisms in thermocapillary liquid bridges. *Phys. Fluids* **7**, 912.

https://doi.org/10.1017/S0022112096004727 Published online by Cambridge University Press